

1 **Rare Earth Doped Metal Oxide Sensor for the Multimodal Detection**
2 **of Volatile Organic Compounds (VOCs)**

3 Matteo Fois, Timothy Cox¹, Norman Ratcliffe, Ben de Lacy Costello*

4 *Department of Applied Sciences, The University of the West of England, Bristol BS16*
5 *1QY, U.K.*

6 ¹*Institute of Biosensing Technology, The University of the West of England, Bristol*
7 *BS16 1QY, UK.*

8 **Corresponding author: Ben de Lacy Costello, Ben.DeLacyCostello@uwe.ac.uk*

9

10 **Abstract**

11 Heated metal oxide sensors have been widely studied for their ability to give a
12 reversible change in the electrical resistance following the interaction with a volatile
13 compound. Another feature is their inherent cataluminescence (CTL) properties when
14 these materials interact with specific volatiles.

15 This study reports for the first time a zirconium oxide nanomaterial doped with a rare
16 earth metal which gives combined resistance and cataluminescence responses, providing
17 enhanced sensitivity and selectivity of detection via a **multimodal response in a single**
18 **sensor**. The europium-doped zirconium oxide, $\text{ZrO}_2:\text{Eu}^{3+}$ was studied and compared
19 with the undoped zirconium oxide, ZrO_2 , and tungsten oxide, WO_3 . Materials were
20 characterised structurally and tested with a series of volatiles. Both the
21 cataluminescence light emission and the resistance response were recorded at different
22 temperatures (starting from 180°C up to 400°C) and then combined to achieve the dual
23 modality response. Europium-doped zirconium oxide gave a better sensitivity in terms
24 of cataluminescence response than the undoped zirconium oxide sensor; dual modality
25 sensing is demonstrated for ethanol and acetone which give cataluminescence and
26 resistance responses on both the undoped and europium doped zirconia.

27

28 **Keywords**

29 Gas sensing; multimodal; cataluminescence; rare-earth ions; metal oxide

30 semiconductors; zirconium dioxide.

31

32 **1. Introduction**

33 Interest in the selective detection of volatile organic compounds at low concentrations
34 (VOCs) has increased over the past decade. Detecting VOCs is of crucial importance in
35 different fields such as environmental monitoring[1,2], medical diagnosis[3–5], air
36 quality monitoring [6–8] and industrial safety and security applications[9]. In the case
37 of security applications, the detection of low concentrations (typically ppb levels) of
38 explosives in air has become of increasing interest due to the heightened threat of
39 international terrorism. [10–12]

40 Among the many detection techniques developed to meet this need, chemical-based
41 sensor systems have a leading role and, in particular, semiconductor metal-oxide gas
42 sensors[13–15]. Detection is typical via a change in their electrical resistance properties
43 allowing high sensitivity but often with limited selectivity. However, this can be
44 improved by doping, the temperature of operation and the use of nanostructured
45 materials. The primary materials studied are typically oxides of yttrium, tin, zinc,
46 tungsten, titanium, and zirconium[16–21].

47 Another property of a sub-class of metal oxide-based materials that have been utilized
48 albeit, less frequently in sensing applications, is their ability to give chemiluminescence,
49 i.e. light emission as a result of the interaction with a target compound. A particular
50 kind of chemiluminescence, called cataluminescence (CTL) has been reported which
51 arises from the heterogeneous catalytic reaction occurring on the surface of solid
52 catalyst accompanied by light emission[22]. It has been reported that the doping of the
53 metal oxides with certain rare earth metals gives an increase in the production of CTL.
54 In particular, europium, terbium and erbium have been employed successfully to
55 enhance the CTL sensitivity of certain metal oxides such as zirconium oxide [23].

56 Although these sensors display high sensitivity of detection for a range of gases, this
57 aspect is accompanied by a lack of specificity of detection. Another practical issue
58 exhibited by these devices is thus the high false alarm rate, especially when the sensors
59 need to be employed in a real-life environment such as explosives detection[25,26].

60

61 A possible solution, to create a sensor with enhanced selectivity, is via a sensor which
62 simultaneously detects both the light emission (CTL) and the electrical resistance.

63 Another important aspect is the sign of response: (i) the change in resistance can be
64 positive or negative depending on the target gas (oxidising /reducing) or the sensor
65 material properties (n-type/p-type), providing further differentiation between two
66 compounds. (ii) the light emission signal can be positive or absent.

67 Nanoparticle-based sensor systems have shown better performance than those fabricated
68 with non-nano materials. These studies [27–29] have optimised the selectivity of a zinc
69 oxide-based resistive sensor for acetone with respect to ethanol by using dumbbell like
70 zinc oxide nanoparticles and varying the operating temperature. Whilst selective to
71 acetone, the sensor is not able to distinguish between a low concentration of acetone or
72 a higher concentration of ethanol. The addition of a second sensing modality, such as
73 CTL, would facilitate such a differentiation to be made. Thus, this paper reports the
74 tests conducted to determine the best sensitivity and selectivity conditions for detection
75 of acetone (the target) and ethanol (the interferent) for a nano-particle europium-doped
76 ZrO_2 dual modality sensor, as compared with an undoped ZrO_2 sensor and a tungsten
77 oxide sensor, included as a standard resistance-based sensor. Different operating
78 temperatures and different targets and interferents have also been studied. To our

79 knowledge, this is the first report in the scientific literature of such a dual modality
80 sensor based on combined resistance and cataluminescence measurements.

81

82 **2. Methods**

83 2.1 Synthesis of the mixed metal oxide $\text{ZrO}_2:\text{Eu}^{3+}$

84 The synthesis of the mixed metal-oxide $\text{ZrO}_2:\text{Eu}^{3+}$, (europium 5 atomic per cent with
85 respect to zirconium) is via a wet chemical method analogous to the one reported in the
86 previous literature[23]. The chemicals utilized for the preparation were of analytical
87 grade and used as received from the suppliers: $\text{ZrO}(\text{NO}_3)_2$ (Aldrich); $\text{Eu}(\text{NO}_3)_3(\text{aq})$;
88 $\text{NH}_4\text{OH}(\text{aq})$ (5M) (Fluka).

89 2.5 mL of a 0.02 M $\text{Eu}(\text{NO}_3)_3(\text{aq})$ solution was added to 10 mL of a 0.1 M $\text{ZrO}(\text{NO}_3)_2(\text{aq})$
90 solution and stirred rapidly. 0.1M $\text{NH}_4\text{OH}(\text{aq})$ was added in a steady stream until the
91 reaction mixture reached pH 8. The precipitate formed was filtered and washed three
92 times with deionised water and the pH adjusted to pH 8 with 0.1M $\text{NH}_4\text{OH}(\text{aq})$. The
93 precipitate was first dried in an oven at 60°C and finally calcined in a muffle furnace for
94 3 hours at 600°C.

95

96 2.2 Characterization

97 Transmission electron microscope (TEM) images were captured using a Philips CM10
98 TEM, 100kV, with a Gatan Orius SC100 (model 832) digital camera.

99 The metal-oxide nanoparticles were also characterised using a scanning electron
100 microscope (SEM), operating at 30kV, combined with EDX using an FEI Quanta 650
101 field emission SEM. Three different detectors were used: Large Field Detector (LFD),

102 Gaseous Secondary Electron Detector (GSED) and Gaseous Back Scattered Electron
103 Detector (GBSD).

104 The composition of the nanoparticle materials was determined using Energy Dispersive
105 X-Ray Microanalysis (EDX), using an Oxford Instruments AZtec Energy EDX system.
106 The voltage used was between 7.5-20 kV.

107 X-Ray Powder Diffraction (XRD) patterns were recorded on a Bruker D2 Phaser in
108 theta-theta geometry using Cu ($K\alpha_1/K\alpha_2$ $\lambda = 0.15418$ nm) radiation and a Ni $K\beta$ filter
109 (detector side). Additional beam optics and settings: primary and secondary axial Soller
110 slits (2.5°), fixed 0.6mm divergence slit, 1mm anti-scatter-screen, Detector: 1D
111 LYNXEYE with a 5° window, Generator: 30kV, 10mA. The software used for the data
112 analysis was the DIFFRAC.SUITE COMMANDER, Bruker AXS. DIFFRAC.EVA 2.1,
113 Bruker AXS (2010-2012).

114 Vibrational Raman spectra and photoluminescence spectra of sensor surfaces were
115 recorded using a Horiba LabRAM HR Evolution Raman Microscope using an Olympus
116 M Plan x5, NA 0.15 objective lens. For Raman scattering measurements, a 785nm laser,
117 ~ 30 mW, was used. For the photoluminescence spectra, excitation was with a 532nm
118 laser, ~ 0.3 mW.

119 For Cataluminescence and Photoluminescence measurements, the sensor was packaged
120 in a dye cast box with an optical window; vapour samples were input to the sensor
121 chamber to obtain cataluminescence spectra.

122 Cataluminescence spectra were recorded using an EG&G 1460 OMA system including
123 a 0.25m Jarrell Ash 82-497 polychromator, 300 lines/mm grating, and 1254 intensified
124 silicon detector cooled to -20° and an accumulation time of 20 seconds. The sensor was
125 placed immediately in front of the polychromator entrance slit. The experimentally

126 determined black body radiation (BBR) from the heated sensor was subtracted from the
127 total emission spectrum to yield the cataluminescence spectrum.

128

129

130 2.3 Sensor Preparation

131 The sensor substrate was a 3 mm x 3mm square alumina tile. On the sensor (front) face
132 was screen printed two gold interdigitated electrodes (four pairs of interpenetrating bars,
133 electrode gap 100 μm). On the reverse face was a platinum heater track which also
134 served as a temperature sensor. The sensor/heater assembly was wire bonded to a TO39
135 transistor can. The resistance of the platinum heater at different temperatures was
136 determined by placing the sensor in an oven whose temperature could be varied. In
137 operation, a feedback control loop was used to maintain the sensor at the required preset
138 temperature.

139 All the sensors were fabricated using a drop-coating method to apply the sensor material
140 to the interdigitated electrodes: a small amount (0.2g) of the metal-oxide was placed in a
141 glass vial, and sufficient water (0.4 g) was added to produce a thick slurry by stirring.

142 The heater resistance at room temperature was of 10 Ohms. Other resistance heater
143 features are reported in the supplementary information. The sensor was prepared by
144 drop coating the oxide paste on to the top surface of the sensor substrate (3 x 3 mm
145 alumina tile) so that it completely covered the interdigitated gold electrodes. The sensor
146 was then allowed to dry at room temperature for 12 hours before use.

147

148 2.4 Experimental

149

150

151 The sensor was housed in a light-tight chamber of volume 100 mL with input and
152 output tubes (internal diameter of 3 mm). Laboratory air was flowed through the
153 chamber using a KNF-Neuberger micro diaphragm pump at a rate of 100 mL/min.
154 The concentrations were validated by the volatile compounds of interest were diluted
155 from headspace concentrations and then injected into the input air flow using a 10mL
156 gas-tight syringe via a silicone rubber septum attached to the inlet tubing of the sensor
157 chamber. At this constant flow rate, the volatile is input to the sensor chamber and
158 mixed, i.e. diluted, with the flowing laboratory air in a few seconds. The concentrations
159 quoted at the sensor are the diluted values achieved at the sensor surface. Compounds
160 characterised by a shallow headspace concentration (under 1 ppm) were generally
161 heated in a thermostatic oven, and the new enhanced headspace concentration was
162 calculated using the Clausius Clapeyron equation. The concentrations in Table 1 are
163 theoretical values based on the vapour pressure of the test substance. To establish the
164 validity of using diluted headspace concentrations the method was tested using selected
165 ion flow tube mass spectrometry (SIFT-MS). The results of these tests for acetone are
166 reported in the supplementary information. The sensors were tested under ambient
167 humidity conditions (40-60% R.H.)
168 A number of controls were run such as injecting air (at the appropriate temperature) or
169 water headspace to ensure that the response is due to the target and not just due to
170 changes in humidity, background volatiles, syringe contamination or changes in oxygen
171 partial pressure. The dual modality responses for a given sensor were measured at
172 different sensor operating temperatures (150°C to 450°C) and at a range of different
173 concentrations of the target volatile compounds (low ppb to high ppm).

174 The light (cataluminescence) produced following the reaction occurring on the surface
175 of the sensor was detected by a Hamamatsu photomultiplier (HP7820) used in photon
176 counting mode; quantum efficiency $\sim 20\%$. Output pulses corresponding to incident
177 photons are counted by an ASCEL Electronic AE20401 5.8 GHz Frequency Counter. A
178 650 nm short-pass filter was placed between the sensor and the photomultiplier (see Fig.
179 8(a)) to enhance the ratio of CTL to the black body radiation (BBR) arising from the
180 heated sensor. Generally, three injections of the same concentration of a given
181 compound are made into the chamber, and the cataluminescence response profile was
182 measured.

183 Regarding the resistance, the sensor is connected to a voltage source and the change in
184 current in response to the presence of a volatile compound is monitored via a Keithley
185 Electrometer model 617 and connected through a suitable Picolog: Prologix GPIB-USB
186 (HPIB-USB) analogue to digital converter which is interfaced to a computer running
187 bespoke sensor analysis and signal conditioning software. The applied voltage was of 5 V.
188 For each material was made a single sensor and they have been tested singularly by the dual-
189 modality experiments.

190

191 **3. Results and Discussion**

192 3.1 Materials and Cataluminescence Characterisation

193 Figs. 1(a) and (b) show TEM images of the (a) ZrO_2 and (b) $\text{ZrO}_2:\text{Eu}^{3+}(5\%)$
194 nanoparticles. Regarding the europium-doped zirconium oxide (Fig. 1(b)) it is observed
195 that some agglomerates formed, possibly caused by uncontrolled coagulation during the
196 precipitation process. The formation of such clusters is more evident in comparison with
197 the undoped ZrO_2 , shown in Fig. 1(a). The images also reveal that the nanoparticles are
198 characterized by a narrow particle size distribution and nearly spherical morphology.

199 Average particle size, as calculated by the ImageJ software, was 22 nm for the
200 undoped zirconium dioxide and 15 nm for the europium doped particles. These values
201 are in accordance with those reported in the literature [11].

202 **Fig. 1.a, Fig. 1.b**

203 SEM micrographs are shown in Fig. 2(a) (ZrO_2) and 2(b) ($\text{ZrO}_2:\text{Eu}^{3+}$). If the ZrO_2
204 nanoparticles, shown in Fig. 2(a) are compared with the $\text{ZrO}_2:\text{Eu}^{3+}$ in Fig. 2(b), the
205 formation of clusters is again found for the europium doped material.

206 **Fig. 2.a, Fig. 2.b**

207 The XRD patterns of the undoped ZrO_2 and the europium doped material are shown
208 respectively in Fig.3 and Fig.4.

209 **Fig. 3**

210 **Fig. 4**

211 The Raman spectra are shown in Fig. 5 for the undoped ZrO_2 and the europium doped
212 ZrO_2 materials for excitation at 785 nm.

213 The XRD data are fitted well to a monoclinic phase for the undoped ZrO_2 and the
214 tetragonal phase for the $\text{ZrO}_2:\text{Eu}^{3+}$ (5%) material.

215 Following the assignment of Hui *et al.* 2015 [30] given in their figure 4, the Raman
216 peaks for the monoclinic and tetragonal phases are indicated in our Fig. 5. Reference to
217 our Fig. 5 confirms that the undoped ZrO_2 and Eu^{3+} doped materials are respectively
218 comprised almost entirely of the monoclinic and tetragonal phases, in agreement with
219 the XRD analysis.

220 It was also possible to calculate the average particle size through the Debye-Scherrer
221 equation $D_c = K\lambda/\beta\cos\theta$ where D_c is the average particle size, K is the Scherrer
222 constant taken to be equal to 0.94, the X-Ray source wavelength is 0.15418 nm, β is the

223 full width at half-maximum of the peak at a diffraction angle of θ . The average particle
224 size calculated for the undoped oxide was 17 nm and that for the Europium-doped was
225 21 nm. These values are in accordance with the values calculated from the TEM images
226 and those reported in the previous literature [11].

227 The Energy Dispersive X-ray Analysis (EDX) pattern for the undoped ZrO_2 is shown in
228 Fig. 6; for this experiment, a voltage of 20kV was used.

229 **Fig. 6**

230 The pattern shown in Fig. 6 identifies the presence of only zirconium and oxygen;
231 whereas EDX analysis of the $\text{ZrO}_2:\text{Eu}^{3+}$ material (Fig. 7) shows that effective doping
232 with europium had been achieved.

233 **Fig. 7**

234 The photoluminescence (PL) spectrum for the $\text{ZrO}_2:\text{Eu}^{3+}$ material is shown in Fig. 8(c),
235 recorded at a sensor temperature of 450°C . The two major PL peaks are at 592 and 607
236 nm. Hui et al recorded PL spectra for ZrO_2 doped with Eu^{3+} with concentrations in the
237 range 0.5 to 5%. Reference to figure 7 of Hui et al shows that, for PL excitation at 254
238 nm, they observed principal PL peaks at similar positions, i.e. 593 and 608 nm; and
239 when their material was doped with at least 3% Eu^{3+} , their PL lineshapes were similar to
240 those we found for our europium doped zirconium dioxide.

241

242 Cataluminescence spectra are shown in Fig. 8 for the interaction of acetone vapour (2
243 parts per thousand) with (a) undoped ZrO_2 and (b) $\text{ZrO}_2:\text{Eu}^{3+}$ also at a sensor
244 temperature of 450°C . The cataluminescence spectrum from $\text{ZrO}_2:\text{Eu}^{3+}$ is similar to that
245 of the corresponding photoluminescence spectrum recorded at the same temperature

246 (Fig. 8(c)). The cataluminescence spectrum from the undoped ZrO₂ is a broad
247 featureless response over the 400 – 700 nm region recorded.

248 **Fig 8**

249

250

251 3.2 Sensing Experiments

252 The following analytes were tested with the apparatus described above: acetone,
253 ethanol, water, hydrogen peroxide, ethylene glycol dinitrate (EGDN), nitroglycerine
254 (NG), 2,4-dinitrotoluene (DNT) and 2,3-dimethyl-2,3-dinitrobutane (DMNB). All
255 chemicals were of analytical grade and used as received from the suppliers. Table 1
256 shows the gas concentration ranges tested. NG and EGDN were in a safe format: 10%
257 by weight immobilised on diatomaceous earth, Kiieselguhr (desensitised) and supplied
258 by one of the projects sponsors DSTL. The compounds tested are a mixture of VOCs and
259 other compounds which have been linked to explosives and possible interferents which may
260 limit their detection in specific applications.

261 **Table. 1**

262 The data were collected as sensor response (light emission or resistance change) as a
263 function of time. The cataluminescence response was defined by subtracting the black
264 body radiation from the signal registered by the photomultiplier. The resistance signal is
265 reported as relative resistance $R = R_{\text{gas}}/R_{\text{air}}$, where R_{gas} is the sensor resistance in the
266 presence of the volatile under investigation, while R_{air} is the value in the presence of air.
267 An overview of the ZrO₂:Eu³⁺ responses, both in terms of cataluminescence and
268 electrical resistance, is reported in Table 2. The operating temperature was of 300°C

269 **Table 2**

270 The dual modality response profiles for the $\text{ZrO}_2:\text{Eu}^3(5\%)$ sensor, at an operating
271 temperature of 275°C , are shown in Fig. 9, for three repeat injections of 296 ppm of
272 acetone. The peak responses are seen to be highly reproducible, i.e. $\sim\pm 5\%$, for both the
273 cataluminescence and resistance responses.

274 **Fig. 9**

275 The sensor gives the response simultaneously in terms of light emission and resistance.
276 Referring to Fig. 9, while the response time is comparable for the two different
277 modalities (~ 10 seconds), the recovery time ($1/e$) is significantly longer (150 seconds)
278 for the resistance measurement vs the cataluminescence response (~ 20 seconds).

279 Fig. 10a shows the light emission response as a function of the concentration of acetone
280 at an operating temperature of 300°C for the three sensor materials. The zirconium
281 oxide sensor and europium doped zirconia sensor have high cataluminescence
282 sensitivity to acetone at this temperature as compared to tungsten oxide sensor, which is
283 at least an order of magnitude lower.

284 Fig. 10b shows more in detail the zirconium oxide and the europium-doped zirconium
285 oxide response. The europium-doped sensor gives a cataluminescence response which is
286 ~ 5 times that of the undoped zirconium oxide sensor. The convergence at the highest
287 acetone concentrations could be partly due to the saturation of the photon counting
288 system at 10^6 photons per second. This result is consistent with that reported by Zhang
289 *et al.*, 2005, where europium doping was seen to improve the light emission and thus
290 the sensitivity of the zirconia cataluminescence sensor, particularly at lower
291 temperatures.

292 **Fig. 10**

293 Fig. 11 shows the cataluminescence response at different temperatures for a high
294 concentration of acetone (296ppm) for the tungsten oxide sensor, which does give a
295 measurable cataluminescence response, but only at temperatures above 250°C and
296 concentrations above 30 ppm. The maximum CTL signal is 8000, which is
297 approximately one hundred times lower than for the undoped and europium doped
298 zirconium oxide sensors at this concentration (see Fig. 10(b)).

299 **Fig. 11**

300 The sensor performance in terms of selectivity as a function of sensor temperature was
301 also studied. In Fig. 12 the ZrO₂:Eu³⁺ CTL response following the interaction with
302 ethanol (58.7ppm) and acetone (29.6ppm) at different temperatures is reported.

303 **Fig. 12**

304 Fig. 13. shows the ratio of the CTL response to acetone (29.6ppm) to that of ethanol
305 (58.7ppm) for the ZrO₂:Eu³⁺ sensor as a function of temperature. The relative response
306 to acetone (29.6ppm) is higher with respect to ethanol (58.7ppm) despite the lower
307 concentration of acetone at all temperatures. This allows the determination of the
308 optimum operating temperature to obtain maximum selectivity for acetone with respect
309 to ethanol to be identified as 200°C; offering a CTL selectivity for acetone over
310 ethanol, normalized to concentration, of ~20. A low temperature of operation is
311 desirable, and overall, this work has shown that the cataluminescence response is better
312 at lower temperatures when compared to the resistance response.

313 **Fig. 13**

314 Fig. 14 shows the cataluminescence response to nitroglycerine for all three sensors
315 studied. The ZrO₂:Eu³⁺ showed the best sensing performance for 0.63 ppm
316 nitroglycerine in the temperature range of 250-300°C. At 350°C, the cataluminescence

317 response is lost in the noise due to the high background signal due to the black body
318 radiation (BBR). The BBR does limit the use of cataluminescent sensors for low
319 concentrations at higher temperatures of operation. Whilst europium doping has
320 significantly increased the CTL signal with respect to undoped zirconia, it has also
321 shifted the peak cataluminescence response to a higher wavelength where the BBR
322 signal is higher. Selective wavelength filtering could reduce BBR relative to CTL. For
323 example, referring to Fig. 8(b), a 50nm width bandpass filter centred around 610 nm
324 would transmit most of the CTL for $\text{ZrO}_2:\text{Eu}^{3+}$, whilst further reducing the BBR.

325 **Fig. 14**

326 The relative resistance response for the three sensors as a function of the concentration
327 of acetone at an operating temperature of 300°C is reported in Fig. 15.

328 **Fig. 15**

329 In this case, the WO_3 gives by far the most massive change in resistance while the
330 zirconium-based sensors give much smaller responses. However, both the undoped and
331 europium doped zirconia-based sensors do give measurable, albeit smaller, responses as
332 shown in Fig. 16. This aspect indicates that the undoped zirconia sensor gives a more
333 considerable resistance change over a wide range of concentrations of acetone when
334 compared to the europium doped sensor. The main benefit from the perspective of
335 multimodal sensing is that the undoped and doped sensors do give different response
336 profiles, showing that the europium doping has affected both the cataluminescence and
337 resistance responses when compared to the undoped sensor.

338 **Fig. 16**

339 One route to achieving selectivity of detection is to consider the ratio between the
340 cataluminescence and the resistance responses (CTL/Resistance). In Fig. 17, this dual

341 modality ratio response is reported for acetone (29.6 ppm) and ethanol (58.7 ppm) at
342 different temperatures. This graph emphasises that it is possible to get a massive
343 difference in the CTL/resistance ratio between two compounds, in this case, acetone
344 and ethanol (target/interferent) at different temperatures. At 200°C, there is a massive
345 difference, but, at 250°C, the acetone and ethanol ratios are similar. Thus, calculating
346 the CTL/resistance ratio can be one method of improving selectivity in this multimodal
347 sensor, with the temperature of operation chosen to optimise differences in this ratio.

348 **Fig 17**

349

350 *Discussion*

351 We believe that this is the first report in the scientific literature of multimodal sensing
352 combining simultaneous resistance and cataluminescence measurements on the same
353 heated metal oxide sensor. This work has demonstrated that the approach shows
354 promise for enhancing the selectivity of detection. In terms of sensor recovery, this is
355 limited by the resistance response which is much slower than the cataluminescence
356 response. The selective wavelength of detection combined with dopants other than
357 europium chosen to shift the CTL to shorter wavelength might offer a route to
358 increasing the ratio of the CTL signal to BBR noise. This would be particularly useful
359 for high sensor temperatures and low vapour concentrations, where the high BBR
360 background limits CTL signal to noise, thereby extending the operational temperature
361 range for multimodal sensing.

362 A further approach is to combine a number of multimodal sensors in a sensor array to
363 offer additional specificity of detection. Such arrays could feature different
364 nanomaterial sensors operated at different temperatures. Such multimodal micro-

365 hotplate sensor arrays could be manufactured using MEMS (MicroElectroMechanical
366 Systems) technology. An improved understanding of the CTL and resistance sensing
367 mechanisms could also lead to enhanced sensor design.

368 At present, although all sensors studied gave some cataluminescence in addition to
369 resistance changes, there were considerable differences observed between tungsten-
370 based sensors which were better for resistance measurement and zirconium oxide-based
371 materials which gave enhanced cataluminescence responses and smaller resistance
372 responses

373 For the zirconia material, europium doping was shown to be successful in enhancing the
374 cataluminescence response and modifying the resistance response vs the undoped
375 material. This demonstrates the potential to dope other metal oxide materials to produce
376 multimodal sensors with differing cataluminescence and resistance response profiles.

377 The work presented here represents a new type of sensor with potential to improve
378 selectivity for detection of individual VOCs in the presence of other interfering
379 volatiles.

380

381 There are certain limitations to the study presented. However, work was carried out at a
382 range of sensor temperatures to find optimal response to targets for each sensing
383 modality, more complete environmental testing such as altering ambient temperature
384 and humidity is required. It should be noted that these tests were carried out at a typical
385 room humidity (40-60%RH) and not under dry air conditions. Hence, the sensors show
386 relatively good stability across this humidity range. Moreover, the cataluminescent
387 response is not affected by humidity in the same way as resistance-based sensors. We
388 did not observe any cataluminescent response to high levels of humidity. However,

389 cataluminescent sensors are adversely affected by high temperature, and the baseline
390 light emission rises as the temperature increase, especially marked above 300°C.
391 However, it should be noted that with better filtering of background light emission vs.
392 Cataluminescent response which are at distinct wavelengths, then this issue could be
393 resolved.

394 Another limitation is the relative cost of combining two modalities compared to typical
395 metal oxide-based sensors which are relatively cheap. The addition of the requirement
396 to measure CTL response adds bulk and a costly photon counting PMT module.
397 However, there are silicon technologies which are appropriate to replace the PMT
398 module and could realise a miniaturised device in future studies. The need for a light-
399 tight cell is also potentially more costly but we have developed field prototypes based
400 on this sensor relatively inexpensively. The baseline resistance of the dual modality
401 sensors giving the best cataluminescent response is relatively high compared to
402 conventional metal oxide sensors. The need to operate at lower temperatures to negate
403 background effects also exacerbates this. However, this paper reports the first step in
404 developing these sensors, and we have tested a range of conventional metal oxide
405 materials, including tungsten that have some CTL based response. Therefore, we
406 envisage the possibility of new materials being discovered with multimodal responses
407 inherent or being synthesised. Future work would consequently, try to identify new
408 materials and also to better understand the sensor characteristics in order to design
409 better and more selective sensors.

410
411
412

413 **4. Conclusions**

414 We have demonstrated for the first time a multimodal sensor that combines resistance
415 and cataluminescent measurements simultaneously on a single heated metal oxide
416 sensor. We have shown that cataluminescence and resistance measurements can be
417 combined to enhance the selectivity of the sensors to various targets as compared to the
418 single mode sensors.

419 The systematic screening was undertaken using the ZrO_2 , $\text{ZrO}_2:\text{Eu}^{3+}$ and WO_3 sensors
420 showed that it is possible to create a sensor system with increased selectivity by using
421 the dual-modality. It is thus possible to distinguish between different targets that, even if
422 they gave a similar response under one of the sensing modalities, they could provide a
423 different response to the sensing modality. It is possible to exploit dual modality for
424 enhanced sensitivity to the presence of a target as one of the modalities could be
425 optimised for sensitivity to that target.

426 In particular, the europium-doped zirconia sensor has shown a better response in terms
427 of CTL even at a relatively low operating temperature, whilst the resistance response is
428 similar to that of the undoped zirconia.. The WO_3 sensor exhibited the best resistance
429 response even with low concentrations of the target compounds but gave limited light
430 emission, which was only detected at high target concentrations. Therefore, it may be
431 considered unsuitable as a multimodal sensor, but its inclusion in a sensor array could
432 be advantageous.

433

434 **Acknowledgements**

435 This project was funded under the Innovative Research Call in Explosives and
436 Weapons Detection 2016 initiative. This is a Cross-Government programme sponsored
437 by a number of Departments and Agencies under the UK Government's CONTEST
438 strategy in partnership with the US Department of Homeland Security, Science and
439 Technology Directorate.

440 The authors wish to thank Dr Dan Wood and Mr Tony Webb from the Threat
441 Mitigation Technologies department of the Metropolitan Police Service for their
442 invaluable help and guidance during the project.

443 The authors would like to thank David Patton and Sue Hula, The University of the
444 West of England for instruments usage and technical assistance relative to the
445 Transmission Electron Microscopy, the Scanning Electron Microscopy and the Energy
446 Dispersive X-ray Analysis.

447 We would also like to thank Dr Mark Light, University of Southampton, for the X-Ray
448 Diffraction data analysis.

449 The views expressed in this publication are those of the authors and not necessarily
450 those of the funding contributors.

451

452 **References**

- 453 [1] M.S. Kamal, S.A. Razzak, M.M. Hossain, Catalytic oxidation of volatile organic
454 compounds (VOCs) - A review, *Atmos. Environ.* (2016).
455 <https://doi.org/10.1016/j.atmosenv.2016.05.031>.
- 456 [2] J.E. Colman Lerner, M. de los A. Gutierrez, D. Mellado, D. Giuliani, L. Massolo,
457 E.Y. Sanchez, A. Porta, Characterization and cancer risk assessment of VOCs in
458 home and school environments in gran La Plata, Argentina, *Environ. Sci. Pollut.*
459 *Res.* (2018). <https://doi.org/10.1007/s11356-018-1265-2>.
- 460 [3] A.D. Wilson, Application of electronic-nose technologies and VOC-biomarkers
461 for the noninvasive early diagnosis of gastrointestinal diseases, *Sensors*
462 (Switzerland). (2018). <https://doi.org/10.3390/s18082613>.
- 463 [4] A.M. Casas-Ferreira, M. del Nogal-Sánchez, J.L. Pérez-Pavón, B. Moreno-
464 Cordero, Non-separative mass spectrometry methods for non-invasive medical
465 diagnostics based on volatile organic compounds: A review, *Anal. Chim. Acta.*
466 (2019). <https://doi.org/10.1016/j.aca.2018.07.005>.
- 467 [5] A. Pizzini, W. Filipiak, J. Wille, C. Ager, H. Wiesenhofer, R. Kubinec, J. Blaško,
468 C. Tschurtschenthaler, C.A. Mayhew, G. Weiss, R. Bellmann-Weiler, Analysis
469 of volatile organic compounds in the breath of patients with stable or acute
470 exacerbation of chronic obstructive pulmonary disease, *J. Breath Res.* (2018).
471 <https://doi.org/10.1088/1752-7163/aaa4c5>.
- 472 [6] C.S. Lee, Z. Dai, D.H. Kim, H.Y. Li, Y.M. Jo, B.Y. Kim, H.G. Byun, I. Hwang,
473 J.H. Lee, Highly discriminative and sensitive detection of volatile organic
474 compounds for monitoring indoor air quality using pure and Au-loaded 2D
475 In₂O₃ inverse opal thin films, *Sensors Actuators, B Chem.* (2018).

- 476 <https://doi.org/10.1016/j.snb.2018.06.011>.
- 477 [7] P. Arroyo, J.L. Herrero, J.I. Suárez, J. Lozano, Wireless sensor network
478 combined with cloud computing for air quality monitoring, *Sensors*
479 (Switzerland). (2019). <https://doi.org/10.3390/s19030691>.
- 480 [8] M.F. Yassin, A.M. Pillai, Monitoring of volatile organic compounds in different
481 schools: a determinant of the indoor air quality, *Int. J. Environ. Sci. Technol.*
482 (2019). <https://doi.org/10.1007/s13762-018-1838-0>.
- 483 [9] S. Öztürk, A. Kösemen, Z. Şen, N. Kılınc, M. Harbeck, Poly(3-methylthiophene)
484 thin films deposited electrochemically on QCMs for the sensing of volatile
485 organic compounds, *Sensors* (Switzerland). (2016).
486 <https://doi.org/10.3390/s16040423>.
- 487 [10] C. Tudisco, A. Motta, T. Barboza, C. Massera, A.E. Giuffrida, R. Pinalli, E.
488 Dalcanale, G.G. Condorelli, Cavitand-Decorated Silicon Columnar
489 Nanostructures for the Surface Recognition of Volatile Nitroaromatic
490 Compounds, *ACS Omega*. (2018). <https://doi.org/10.1021/acsomega.8b01018>.
- 491 [11] J.R. Askim, Z. Li, M.K. LaGasse, J.M. Rankin, K.S. Suslick, An optoelectronic
492 nose for identification of explosives, *Chem. Sci.* (2016).
493 <https://doi.org/10.1039/c5sc02632f>.
- 494 [12] K. Konstantynovski, G. Njio, F. Börner, A. Lepcha, T. Fischer, G. Holl, S.
495 Mathur, Bulk detection of explosives and development of customized metal
496 oxide semiconductor gas sensors for the identification of energetic materials,
497 *Sensors Actuators, B Chem.* (2018). <https://doi.org/10.1016/j.snb.2017.11.116>.
- 498 [13] A. Dey, Semiconductor metal oxide gas sensors: A review, *Mater. Sci. Eng. B*
499 *Solid-State Mater. Adv. Technol.* (2018).

- 500 <https://doi.org/10.1016/j.mseb.2017.12.036>.
- 501 [14] T. Lin, X. Lv, Z. Hu, A. Xu, C. Feng, Semiconductor metal oxides as
502 chemoresistive sensors for detecting volatile organic compounds, *Sensors*
503 (Switzerland). (2019). <https://doi.org/10.3390/s19020233>.
- 504 [15] D. Nunes, A. Pimentel, A. Goncalves, S. Pereira, R. Branquinho, P. Barquinha,
505 E. Fortunato, R. Martins, Metal oxide nanostructures for sensor applications,
506 *Semicond. Sci. Technol.* (2019). <https://doi.org/10.1088/1361-6641/ab011e>.
- 507 [16] A. Staerz, T. Russ, U. Weimar, N. Barsan, Understanding the Sensing
508 Mechanism of WO₃ based Gas Sensors, in: *ISOEN 2019 - 18th Int. Symp.*
509 *Olfaction Electron. Nose, Proc.*, 2019.
510 <https://doi.org/10.1109/ISOEN.2019.8823145>.
- 511 [17] J. Zheng, T. Zhang, H. Zeng, W. Guo, B. Zhao, Y. Sun, Y. Li, L. Jiang,
512 Multishelled Hollow Structures of Yttrium Oxide for the Highly Selective and
513 Ultrasensitive Detection of Methanol, *Small*. (2019).
514 <https://doi.org/10.1002/sml.201804688>.
- 515 [18] B.P.J. de Lacy Costello, R.J. Ewen, N.M. Ratcliffe, M. Richards, Highly
516 sensitive room temperature sensors based on the UV-LED activation of zinc
517 oxide nanoparticles, *Sensors Actuators, B Chem.* (2008).
518 <https://doi.org/10.1016/j.snb.2008.06.055>.
- 519 [19] L.E. Ocola, Y. Wang, R. Divan, J. Chen, Multifunctional UV and gas sensors
520 based on vertically nanostructured zinc oxide: Volume versus surface effect,
521 *Sensors* (Switzerland). (2019). <https://doi.org/10.3390/s19092061>.
- 522 [20] B. Gökdere, A. Üzer, S. Durmazel, E. Erçağ, R. Apak, Titanium dioxide
523 nanoparticles–based colorimetric sensors for determination of hydrogen peroxide

524 and triacetone triperoxide (TATP), *Talanta*. (2019).
525 <https://doi.org/10.1016/j.talanta.2019.04.071>.

526 [21] U. Guth, H.D. Wiemhöfer, Gas sensors based on oxygen ion conducting metal
527 oxides, in: *Gas Sensors Based Conduct. Met. Oxides Basic Understanding*,
528 Technol. Appl., 2018. <https://doi.org/10.1016/B978-0-12-811224-3.00002-0>.

529 [22] J. Hu, L. Zhang, Y. Lv, Recent advances in cataluminescence gas sensor:
530 Materials and methodologies, *Appl. Spectrosc. Rev.* (2019).
531 <https://doi.org/10.1080/05704928.2018.1464932>.

532 [23] Z. Zhang, K. Xu, W.R.G. Baeyens, X. Zhang, An energy-transfer
533 cataluminescence reaction on nanosized catalysts and its application to chemical
534 sensors, *Anal. Chim. Acta.* (2005). <https://doi.org/10.1016/j.aca.2004.12.025>.

535 [24] M. Hijazi, M. Rieu, V. Stambouli, G. Tournier, J.P. Viricelle, C. Pijolat, Ambient
536 temperature selective ammonia gas sensor based on SnO₂-APTES modifications,
537 *Sensors Actuators, B Chem.* (2018). <https://doi.org/10.1016/j.snb.2017.10.036>.

538 [25] N. Joshi, T. Hayasaka, Y. Liu, H. Liu, O.N. Oliveira, L. Lin, A review on
539 chemiresistive room temperature gas sensors based on metal oxide
540 nanostructures, graphene and 2D transition metal dichalcogenides, *Microchim.*
541 *Acta.* (2018). <https://doi.org/10.1007/s00604-018-2750-5>.

542 [26] S. Zampolli, I. Elmi, J. Stürmann, S. Nicoletti, L. Dori, G.C. Cardinali,
543 Selectivity enhancement of metal oxide gas sensors using a micromachined gas
544 chromatographic column, *Sensors Actuators, B Chem.* (2005).
545 <https://doi.org/10.1016/j.snb.2004.06.036>.

546 [27] M.E. Franke, T.J. Koplin, U. Simon, Metal and metal oxide nanoparticles in
547 chemiresistors: Does the nanoscale matter?, *Small.* (2006).

548 <https://doi.org/10.1002/sml.200500261>.

549 [28] J.M. George, A. Antony, B. Mathew, Metal oxide nanoparticles in
550 electrochemical sensing and biosensing: a review, *Microchim. Acta.* (2018).
551 <https://doi.org/10.1007/s00604-018-2894-3>.

552 [29] Q. Qi, T. Zhang, L. Liu, X. Zheng, Q. Yu, Y. Zeng, H. Yang, Selective acetone
553 sensor based on dumbbell-like ZnO with rapid response and recovery, *Sensors*
554 *Actuators, B Chem.* (2008). <https://doi.org/10.1016/j.snb.2008.04.024>.

555 [30] Y. Hui, B. Zou, S. Liu, S. Zhao, J. Xu, Y. Zhao, X. Fan, L. Zhu, Y. Wang, X.
556 Cao, Effects of Eu³⁺-doping and annealing on structure and fluorescence of
557 zirconia phosphors, *Ceram. Int.* (2015).
558 <https://doi.org/10.1016/j.ceramint.2014.10.091>.

559

560

561

562

563 **Captions to Illustrations**

564 Fig.1 Transmission Electron Microscopy (TEM) images for (a) ZrO₂ and (b) ZrO₂:Eu³⁺
565 nanoparticles.

566 Fig. 2 Scanning Electron Microscopy (SEM) images for (a) ZrO₂ and (b) ZrO₂:Eu³⁺
567 nanoparticles.

568 Fig.3 X-Ray Diffraction (XRD) pattern of the undoped zirconium oxide and relative
569 phase attribution fitting.

570 Fig. 4 X-Ray Diffraction (XRD) pattern and phase attribution fitting for the ZrO₂:Eu³⁺
571 material.

572 Fig. 5 Raman spectrum of undoped ZrO₂ nanoparticles (upper trace) and ZrO₂:Eu³⁺
573 nanoparticles (lower trace). The positions of peaks are marked for the tetragonal phase
574 (t) and monoclinic phase (m), following Hui et al., 2015; i.e. monoclinic at 179 and 190
575 cm⁻¹ and tetragonal at 147, 264, 319, 462 and 642 cm⁻¹.

576 Fig 6. EDX spectrum for undoped ZrO₂ material. The peak positions for Zr and O are
577 marked.

578 Fig. 7 EDX spectrum for ZrO₂:Eu³⁺. The peak positions for Zr, O, and Eu are marked.

579 Fig. 8 Photoluminescence and cataluminescence spectra at 450°C : (a)
580 cataluminescence from undoped ZrO₂ for acetone at 2 parts per thousand (ppth). The
581 dotted line indicates the calculated form of black body radiation (BBR). (b)
582 cataluminescence from ZrO₂:Eu³⁺ for acetone at 2 ppth and (c) photoluminescence from
583 ZrO₂:Eu³⁺ with 532 nm excitation.

584 Fig. 9 Resistance (upper trace) and Cataluminescence (lower trace) responses from the
585 ZrO₂:Eu³⁺ sensor (275°C), for three injections of 296 ppm of acetone.

586 Fig. 10 Cataluminescence response as a function of the concentration of acetone for (a)
587 the three different sensors on a vertical scale and (b) detail of the ZrO₂ and ZrO₂:Eu³⁺
588 sensor responses on a logarithmic vertical scale.

589 Fig. 11 Cataluminescence response for a WO₃ sensor following the interaction with
590 296 ppm of acetone, at different temperatures.

591 Fig. 12 Cataluminescence response from ZrO₂:Eu³⁺ as a function of temperature for
592 ethanol (58.7 ppm), lower trace, and acetone (29.6 ppm), upper trace.

593 Fig. 13 Ratio between acetone (29.6 ppm) and ethanol (58.7 ppm) cataluminescence
594 signals at different temperatures for the ZrO₂:Eu³⁺ sensor.

595 Fig. 14 Cataluminescence response for the three sensors studied for nitroglycerine
596 (0.63 ppm) at different temperatures.

597 Fig. 15 Relative resistance ($R_{\text{gas}}/R_{\text{air}}$) response as a function of the concentration of
598 acetone for the three different sensors studied at 300°C.

599 Fig. 16 Relative resistance ($R_{\text{gas}}/R_{\text{air}}$) response at 300°C for the undoped zirconium
600 oxide sensor (upper trace) and $\text{ZrO}_2:\text{Eu}^{3+}$ (lower trace).

601 Fig. 17 Ratio between the relative CTL signal and the relative resistance signals for
602 acetone (29.6 ppm) and ethanol (58.7 ppm), for the $\text{ZrO}_2:\text{Eu}^{3+}$ sensor as a function of
603 temperature.

604

605

606

607 **Table 1 Volatile organic compounds (VOCs) tested and relative sample vapour**
 608 **concentration**

Sample Vapour Concentrations (ppm)	
Sample	Concentrations (ppm)
Acetone	0.00296 – 296
Ethanol	0.005871 – 58.71
Water	312
Hydrogen Peroxide	1.92
Ethylene Glycol Dinitrate (EGDN) 75°C	0.63
Nitroglycerine (NG) 75°C	0.64
2,4-Dinitrotoluene (DNT) 75°C	0.05 – 0.5
2,3-Dimethyl-2,3-Dinitrobutane (DMNB) 75°C	2.76

609

610

611 **Table 2 Cataluminescence (CTL) and electric resistance response for the**
 612 **ZrO₂:Eu³⁺ sensor, following the interaction with all the VOCs tested at different**
 613 **concentrations. Operating temperature of 300°C.**

Compound	Concentration (ppm)	CTL Response (Hz)	Relative Resistance Response (R_{gas}/R_{air})
Acetone	296	1.35×10^6	133.90
Acetone	29.6	4.42×10^5	22.67
Acetone	2.96	2.80×10^4	3.99
Acetone	0.296	9.61×10^3	2.04
Acetone	2.96×10^{-2}	1.11×10^3	1.21
Ethanol	58.71	1.64×10^5	18.78
Ethanol	5.871	8.10×10^3	1.88
Ethanol	0.5871	3.17×10^3	1.35
Ethanol	5.871×10^{-2}	914.18	1.10
H ₂ O	312	0	1
H ₂ O ₂	1.92	0	1
2,4-DNT	0.543	7.14×10^3	1.77
DMNB	2.76	0	1
EGDN	0.631	1.39×10^3	1.15
NG	0.632	1.86×10^3	1.20

614

615

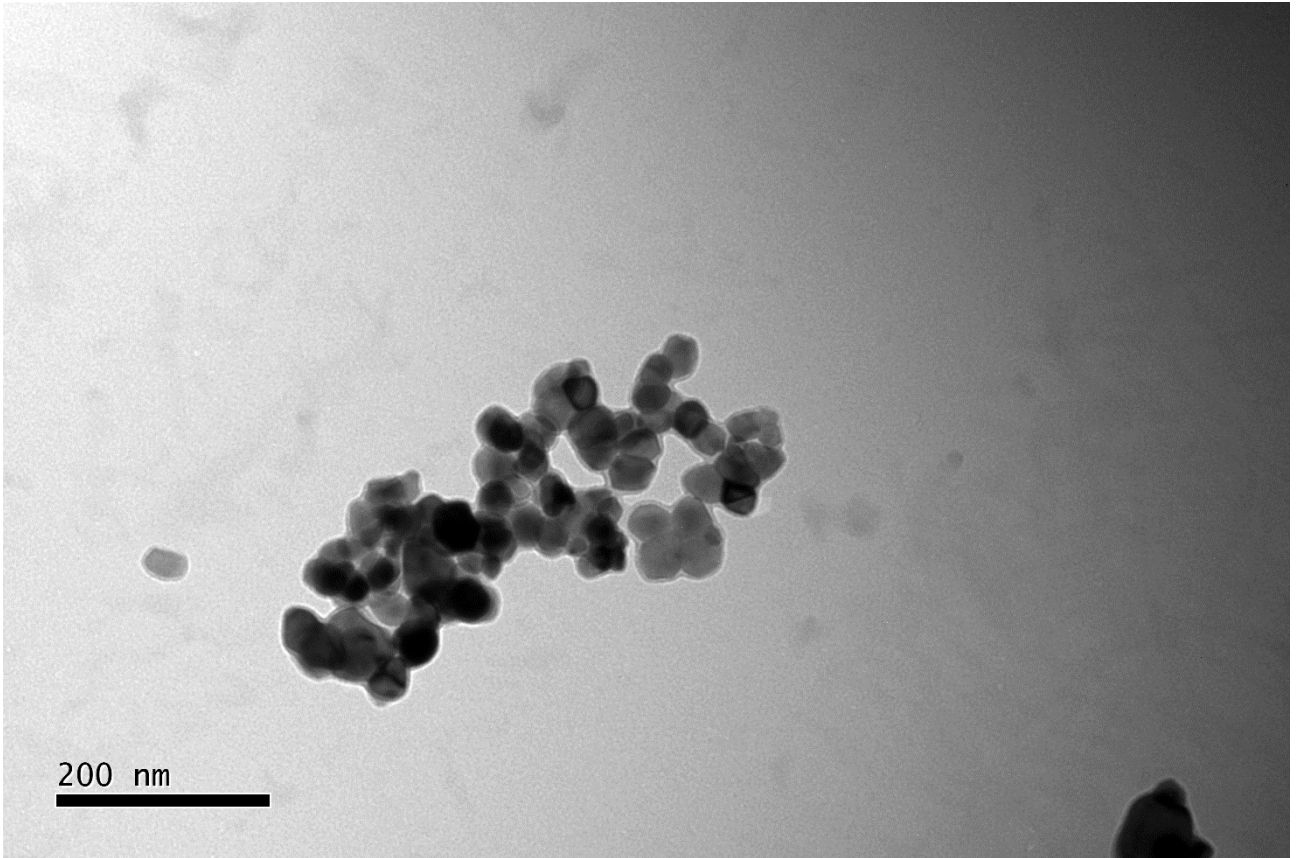
616

617 This research did not receive any specific grant from funding agencies in the public,

618 commercial, or not-for-profit sectors.

619

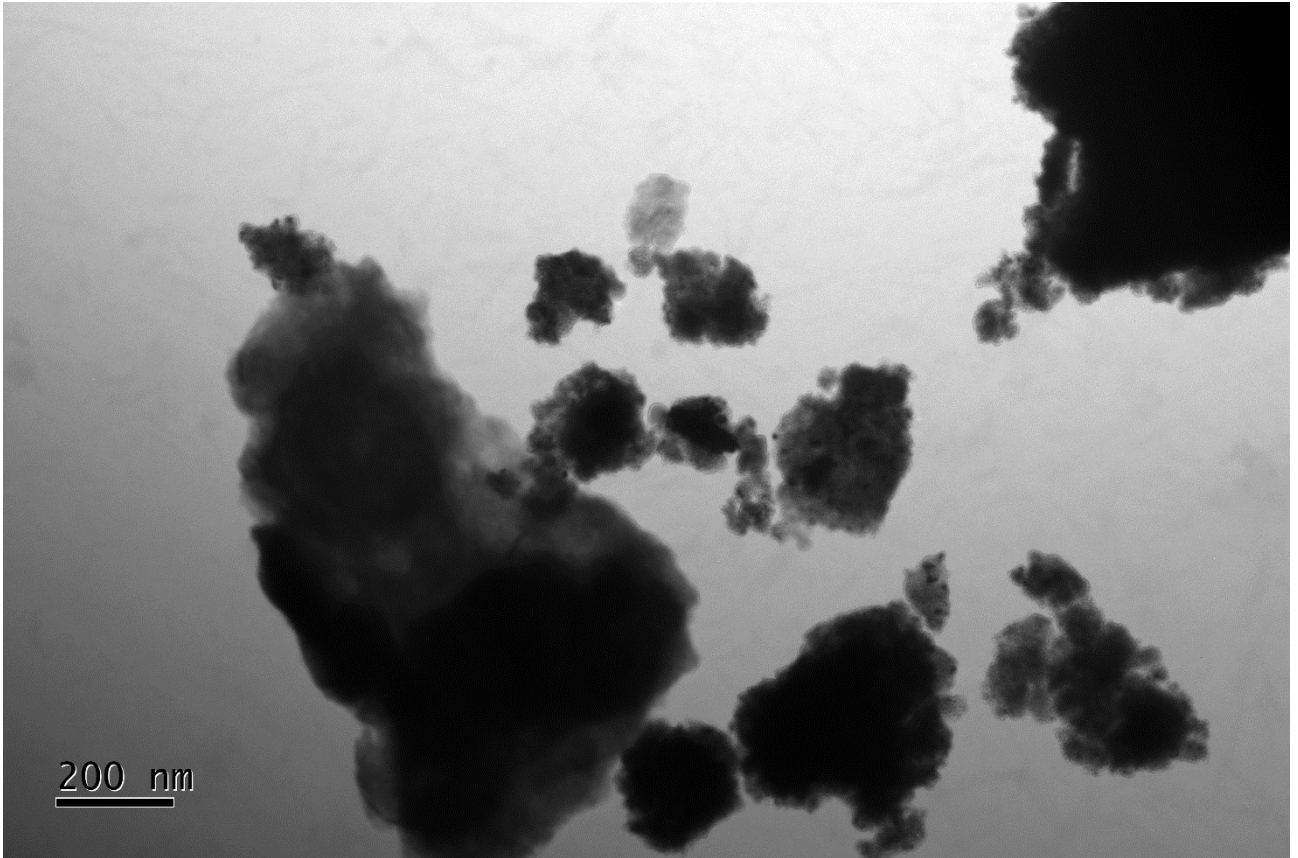
620



621

622 **Fig.1a**

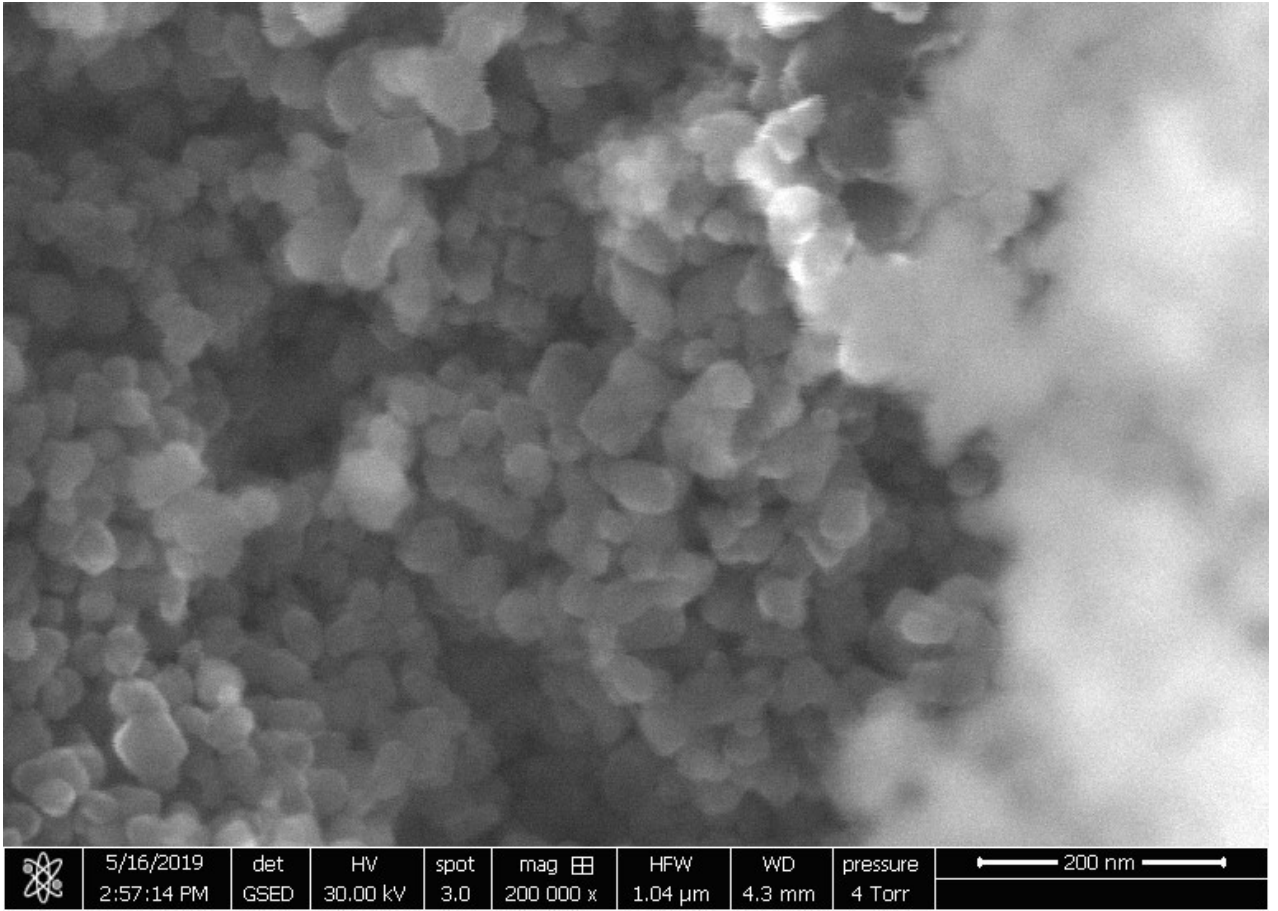
623



624

625 **Fig.1b**

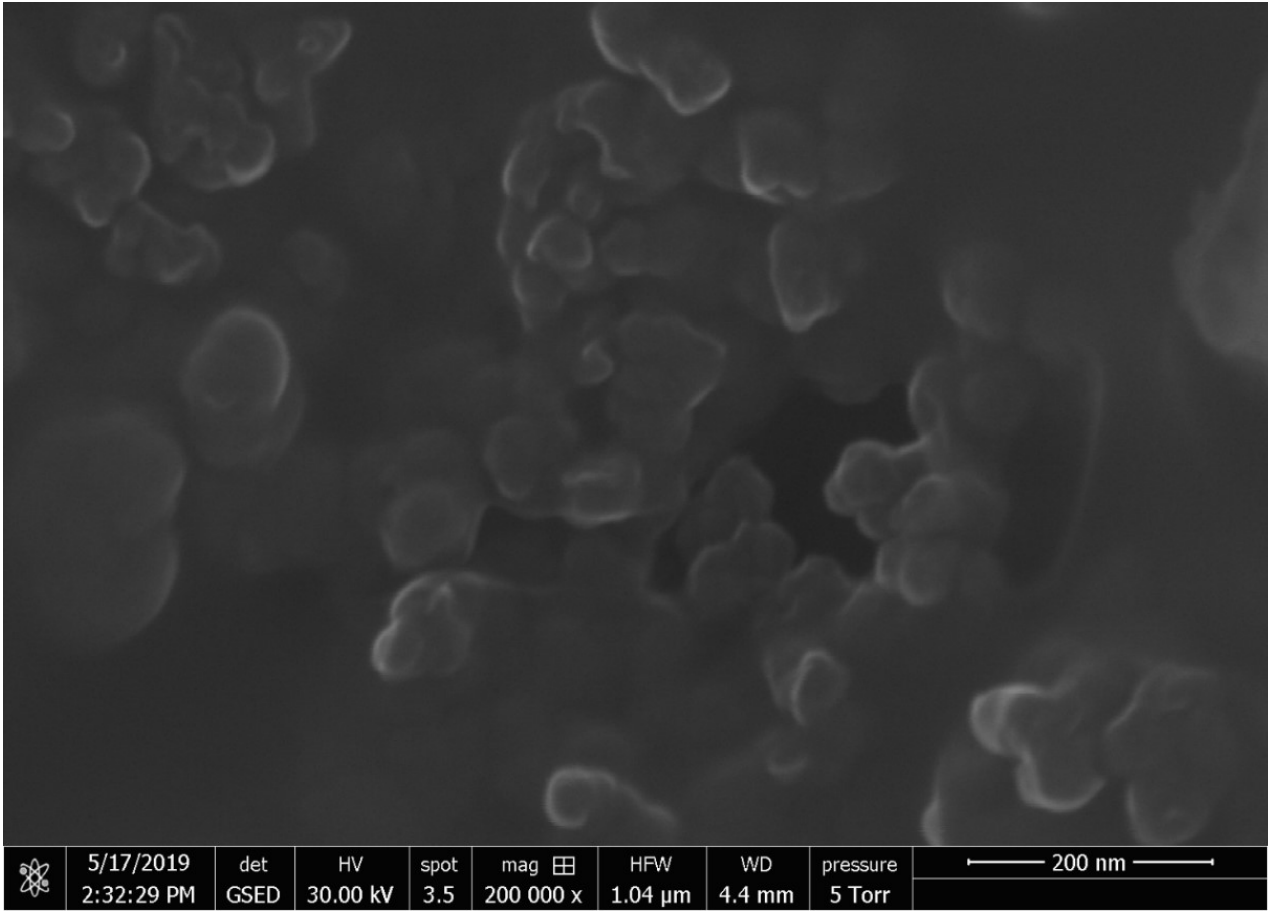
626



627

628 **Fig. 2a**

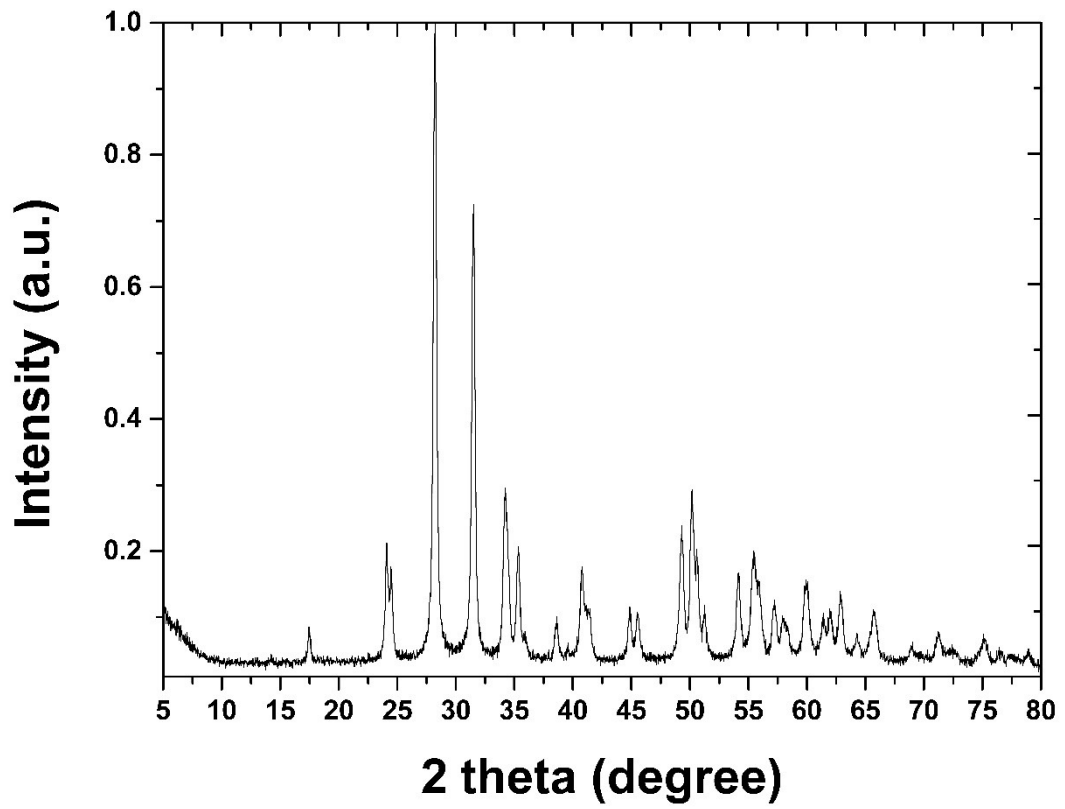
629



630

631 **Fig. 2b**

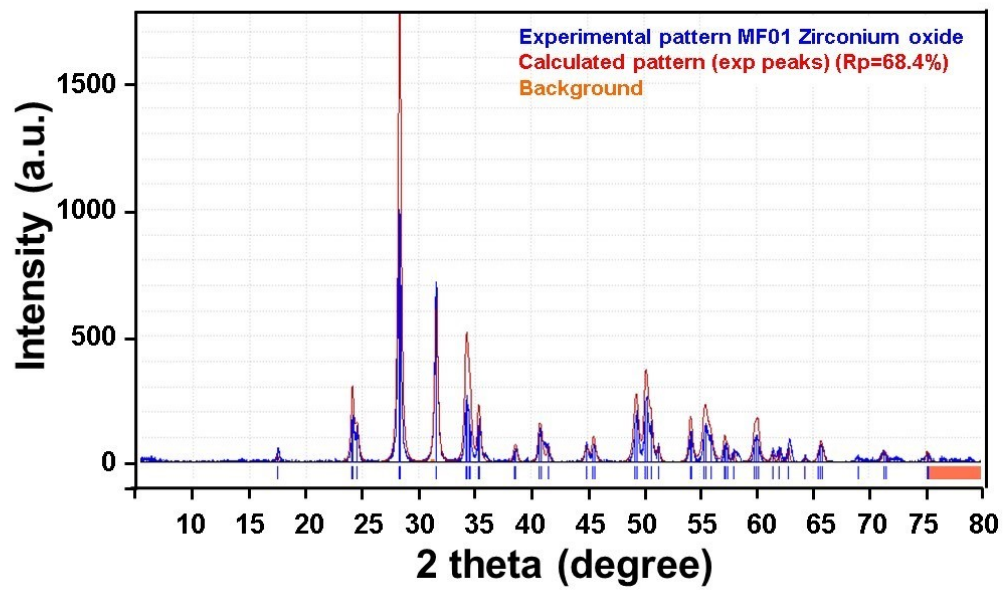
632



633

634 **Fig. 3a**

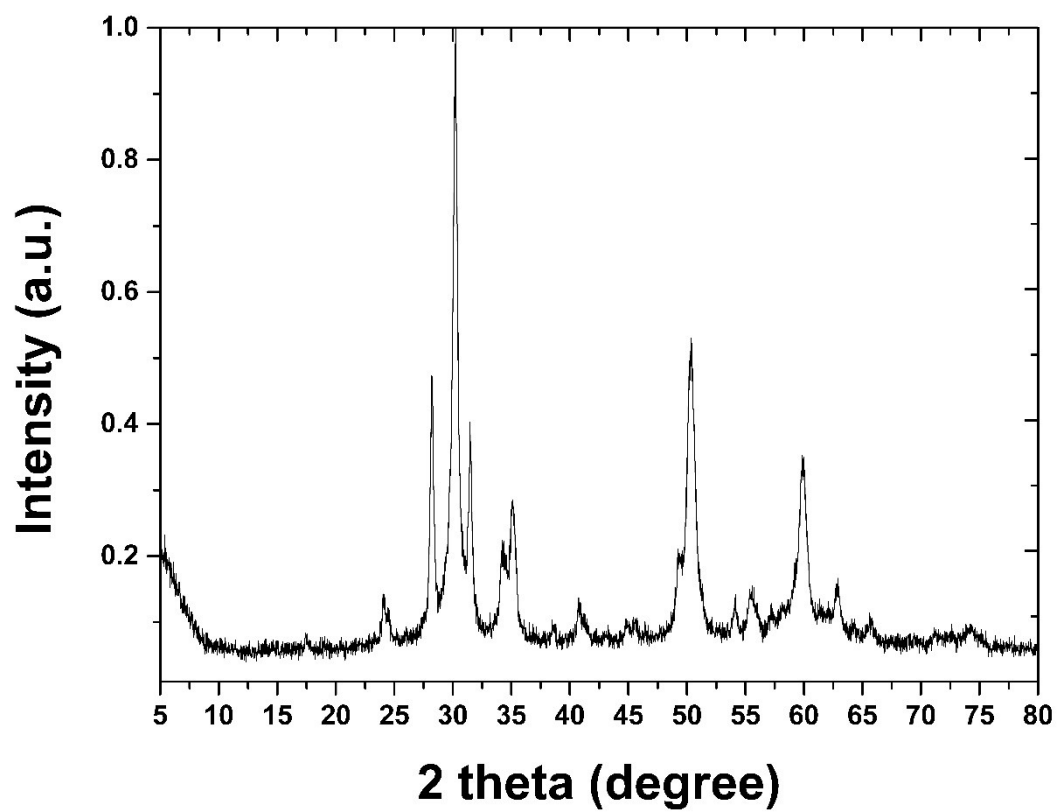
635



636

637 **Fig. 3b**

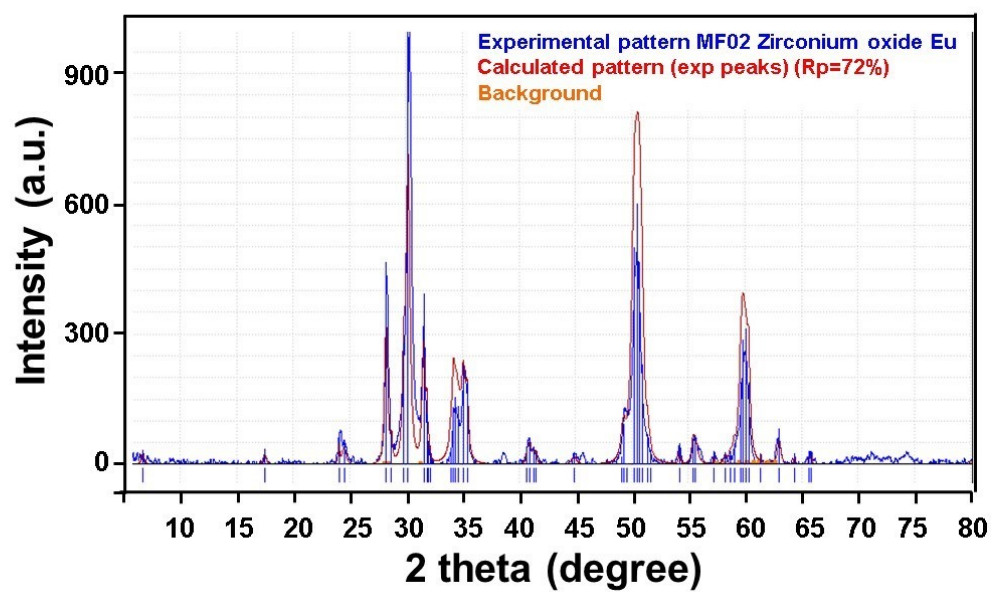
638



639

640 **Fig. 4a**

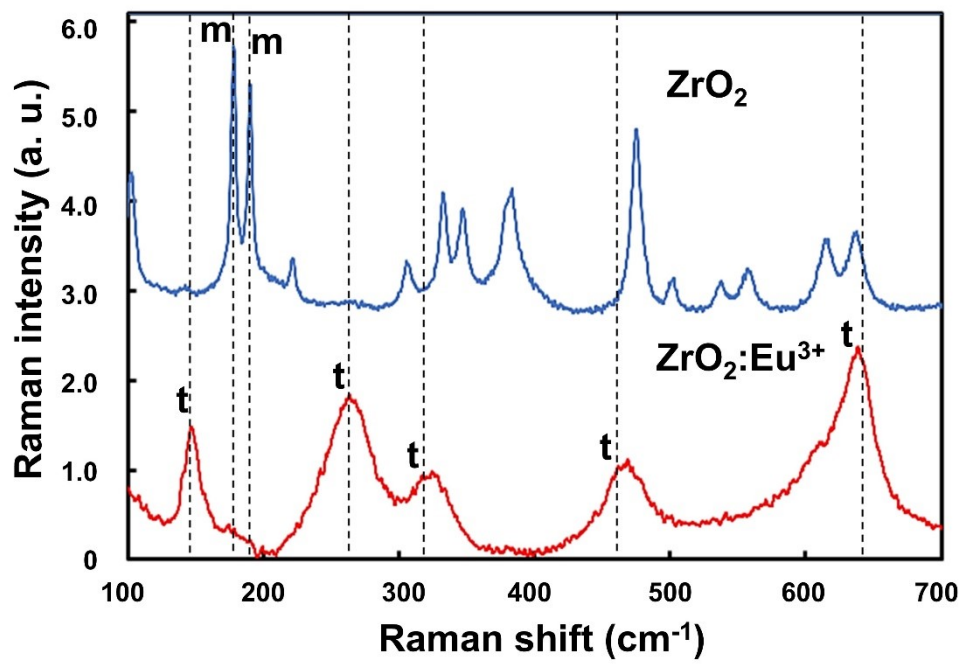
641



642

643 **Fig. 4b**

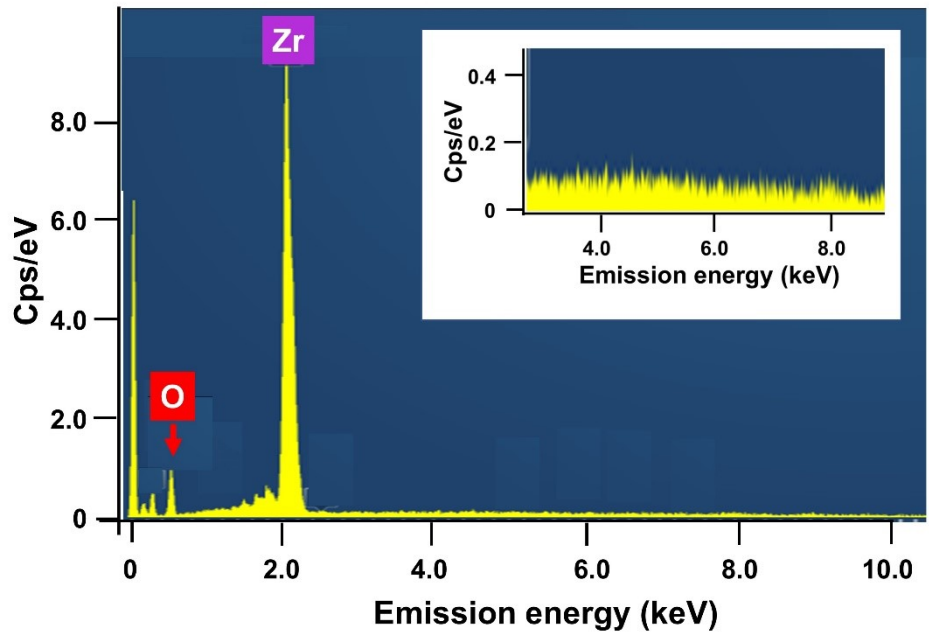
644



645

646 **Fig. 5**

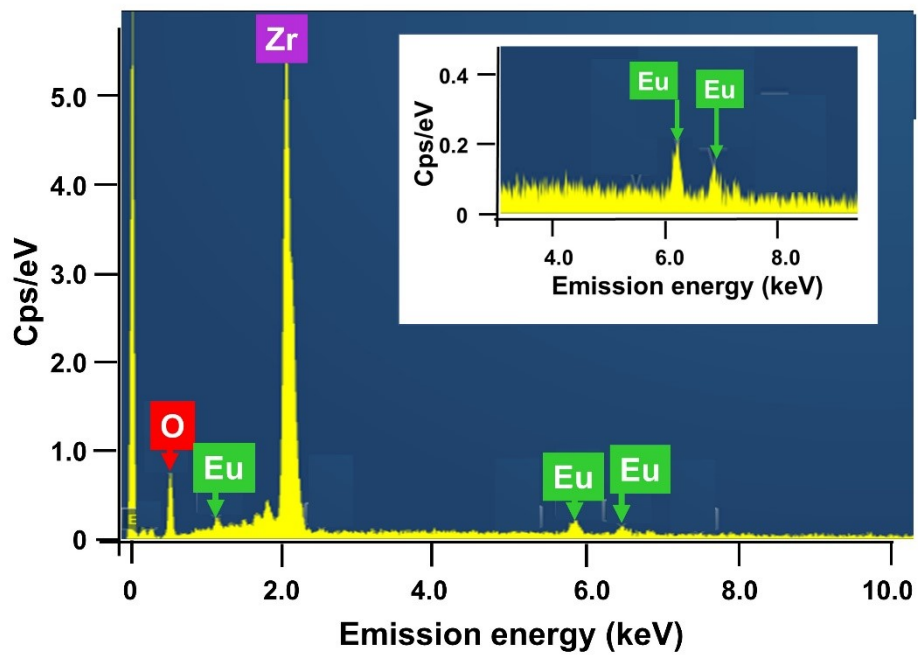
647



648

649 **Fig. 6**

650

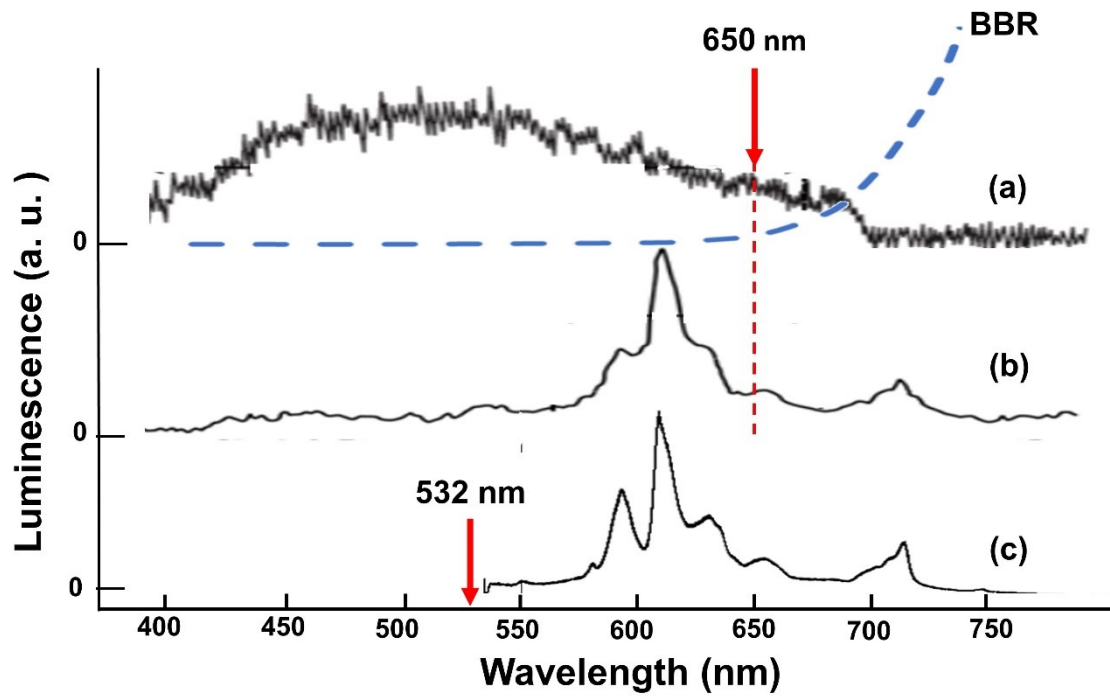


651

652 **Fig. 7**

653

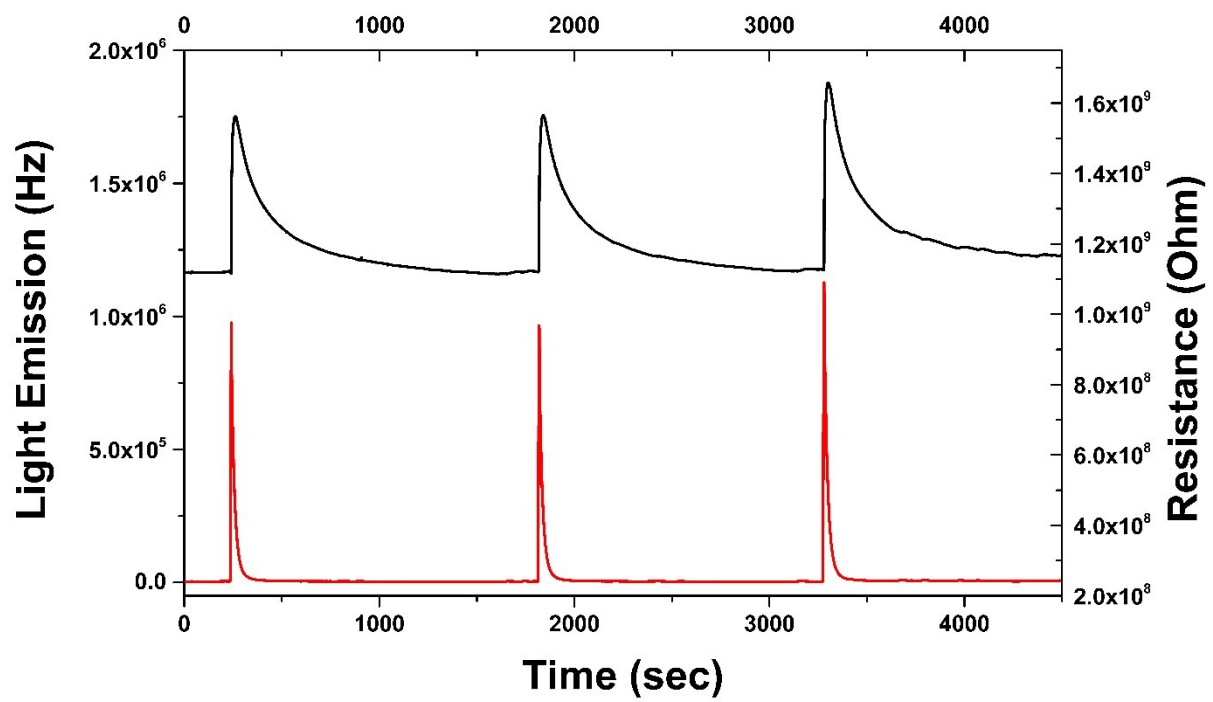
654



655

656 **Fig. 8**

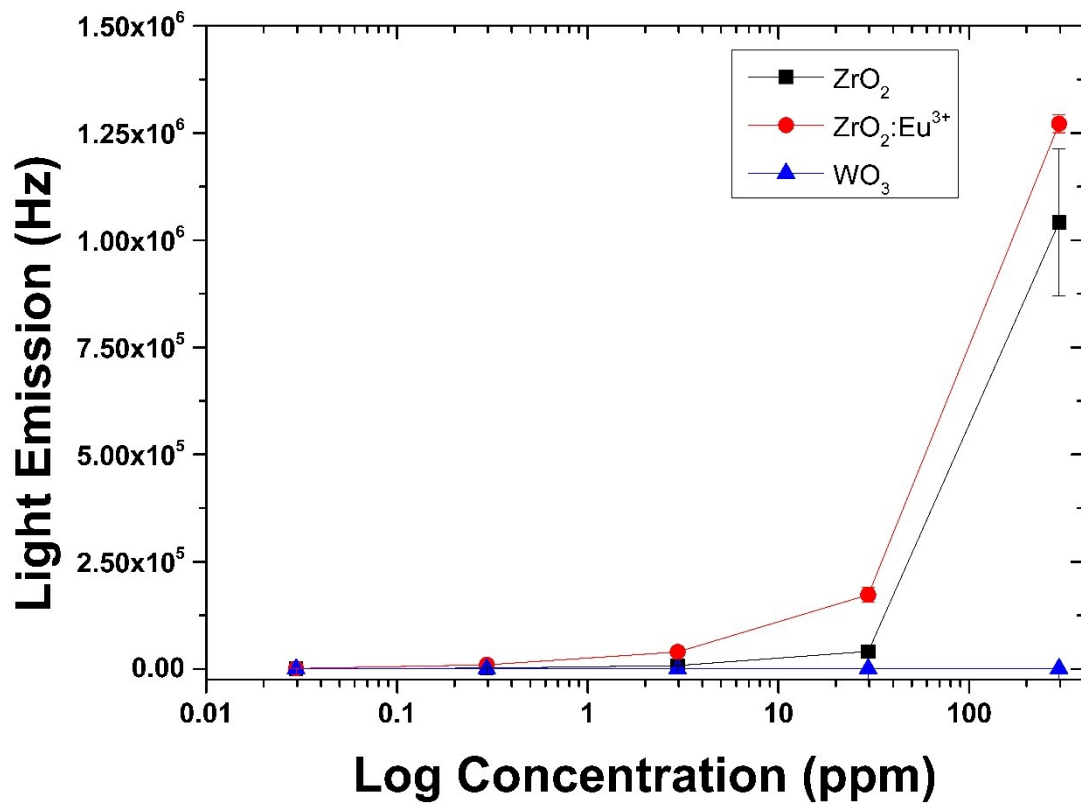
657



658

659 **Fig. 9**

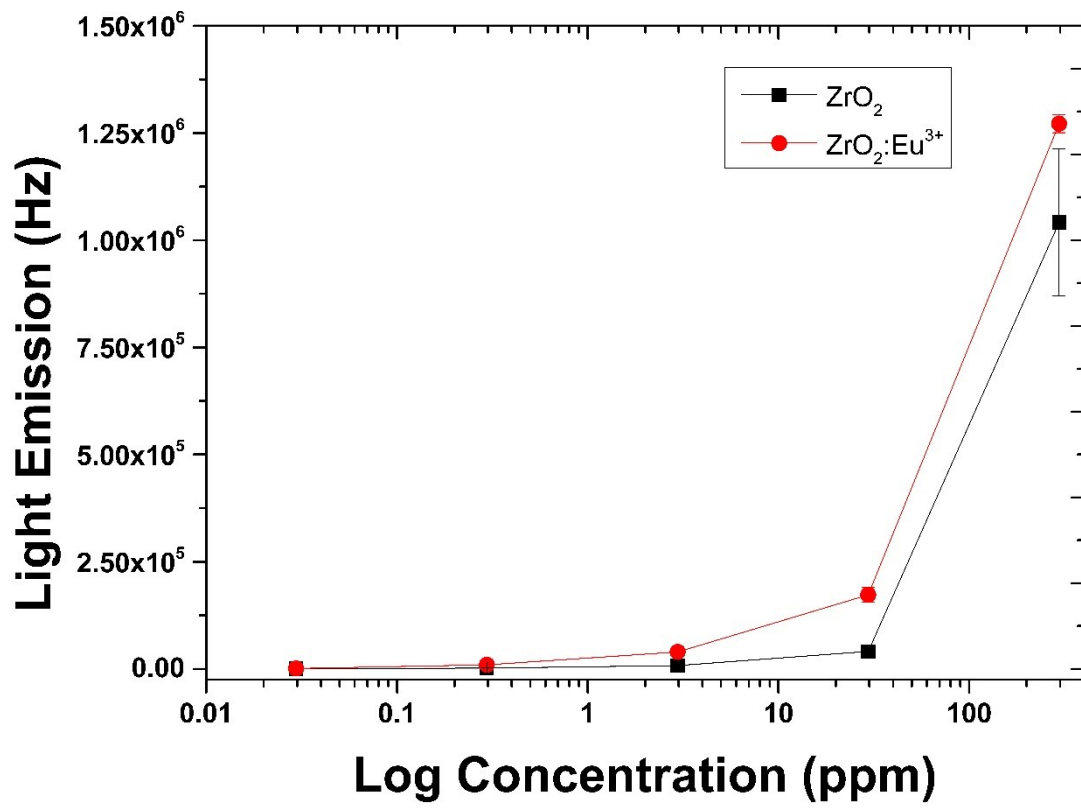
660



661

662 **Fig. 10a**

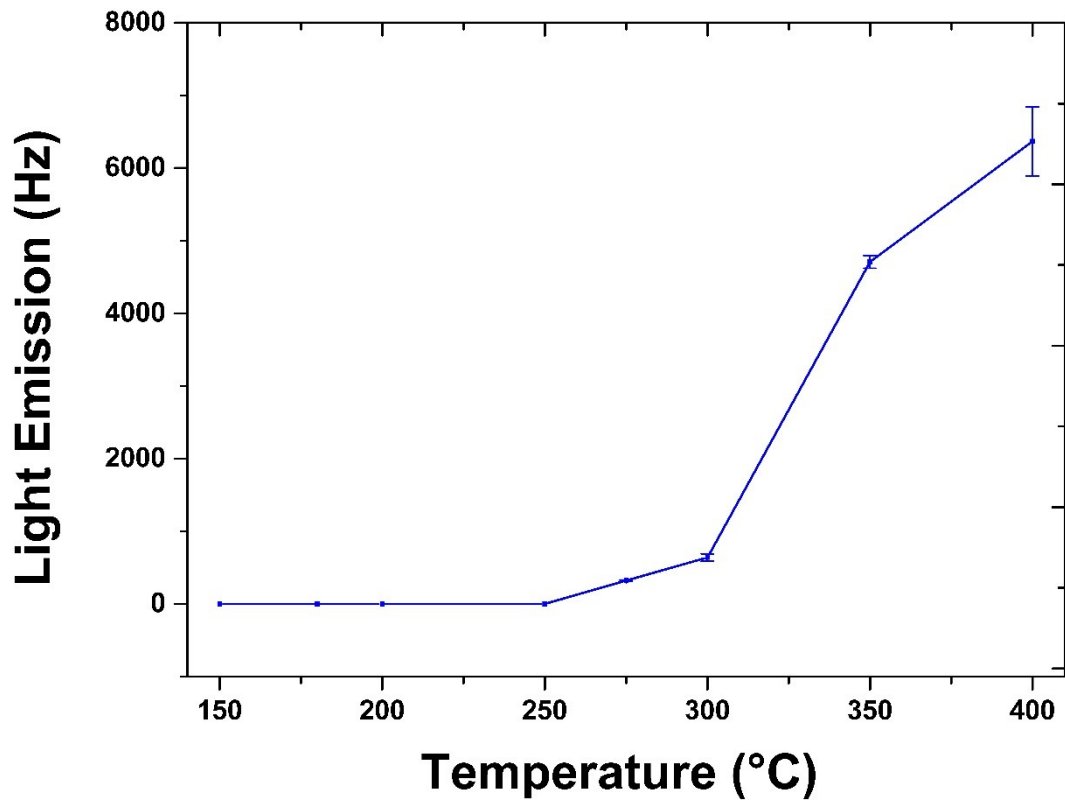
663



664

665 **Fig. 10b**

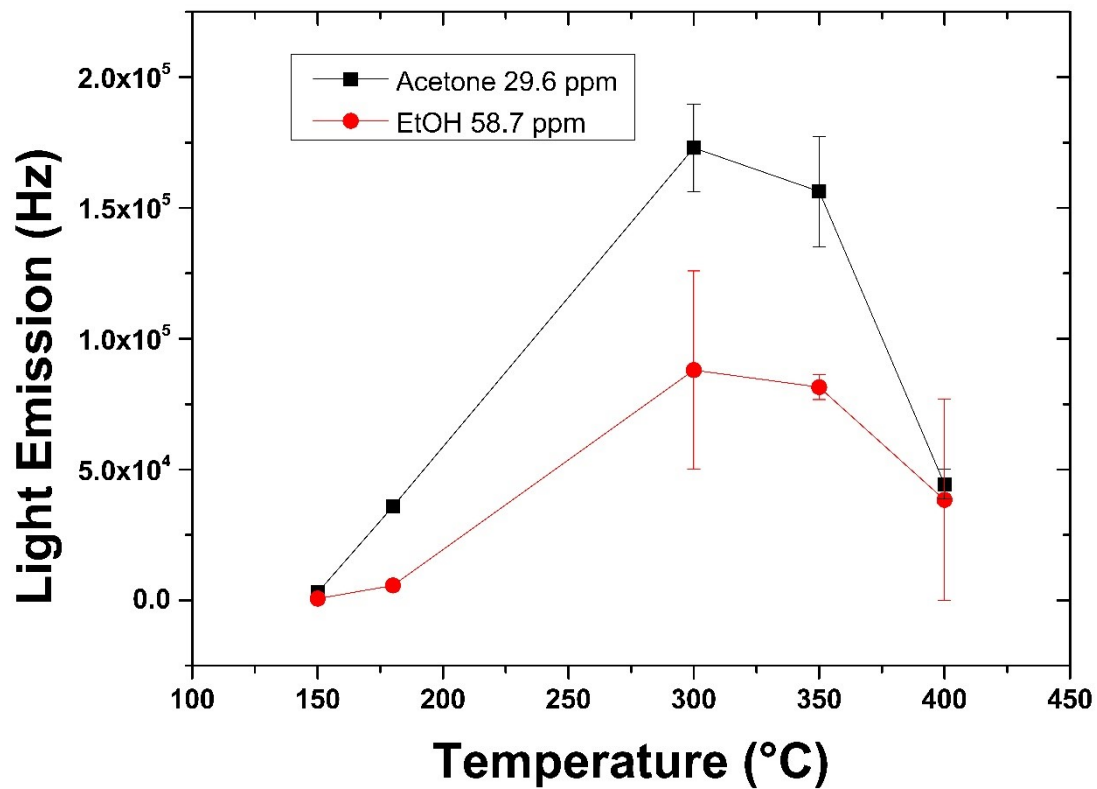
666



667

668 **Fig. 11**

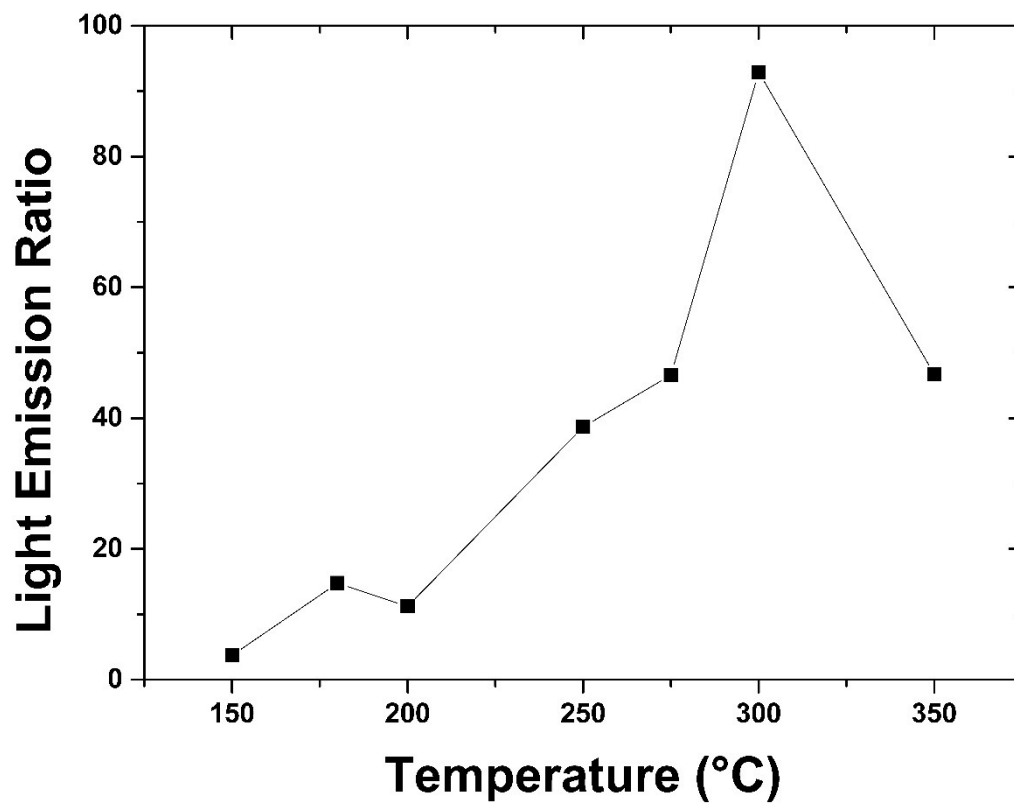
669



670

671 **Fig. 12**

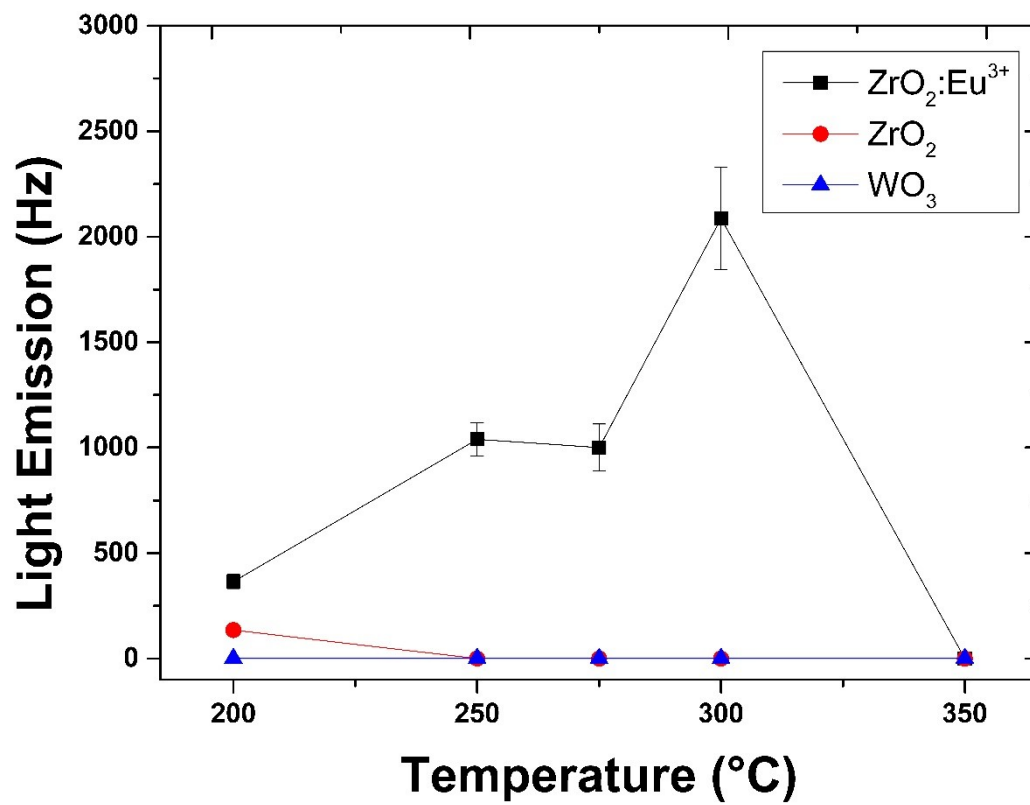
672



673

674 **Fig. 13**

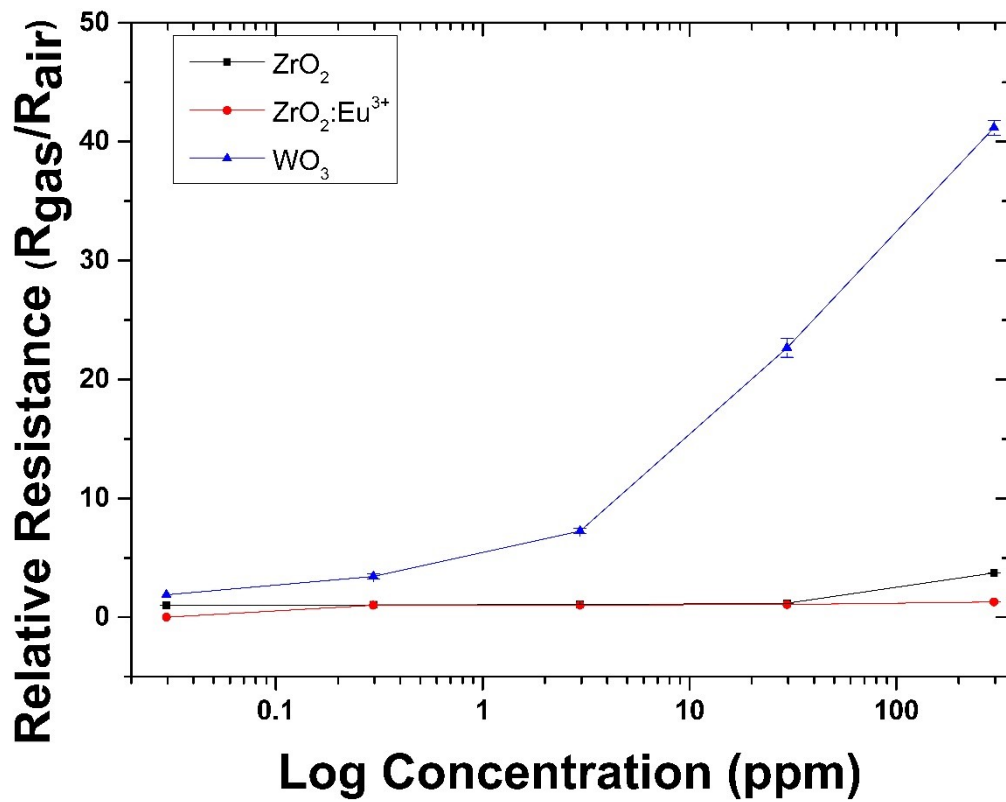
675



676

677 **Fig. 14**

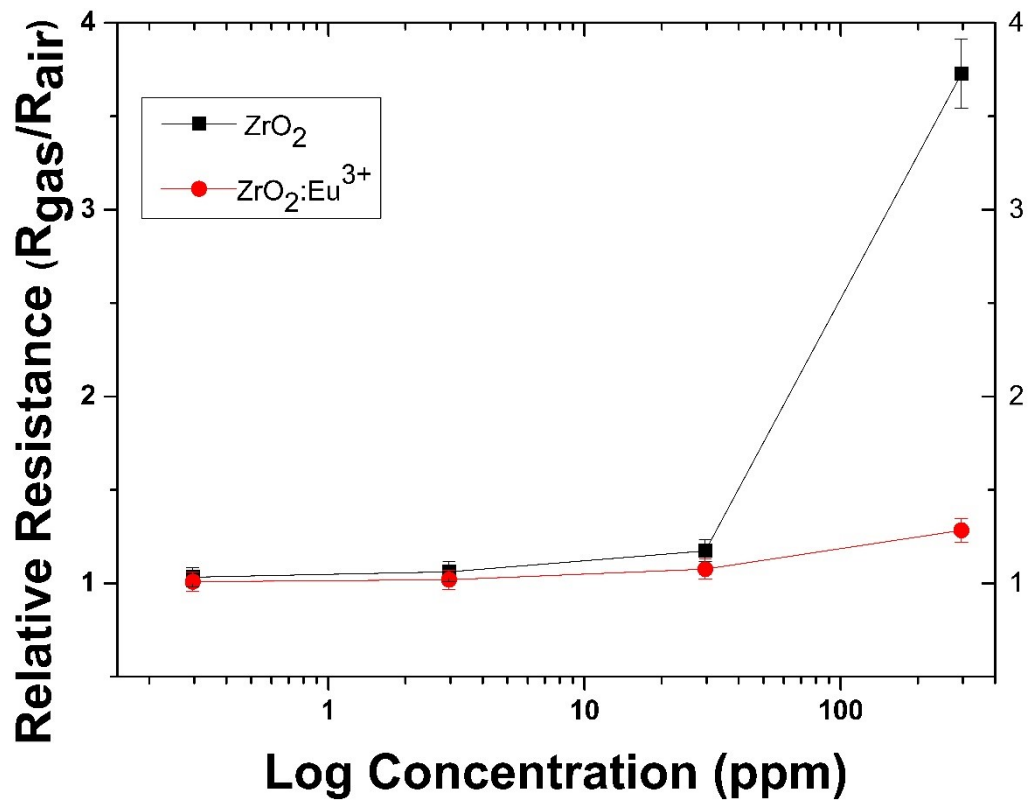
678



679

680 **Fig. 15**

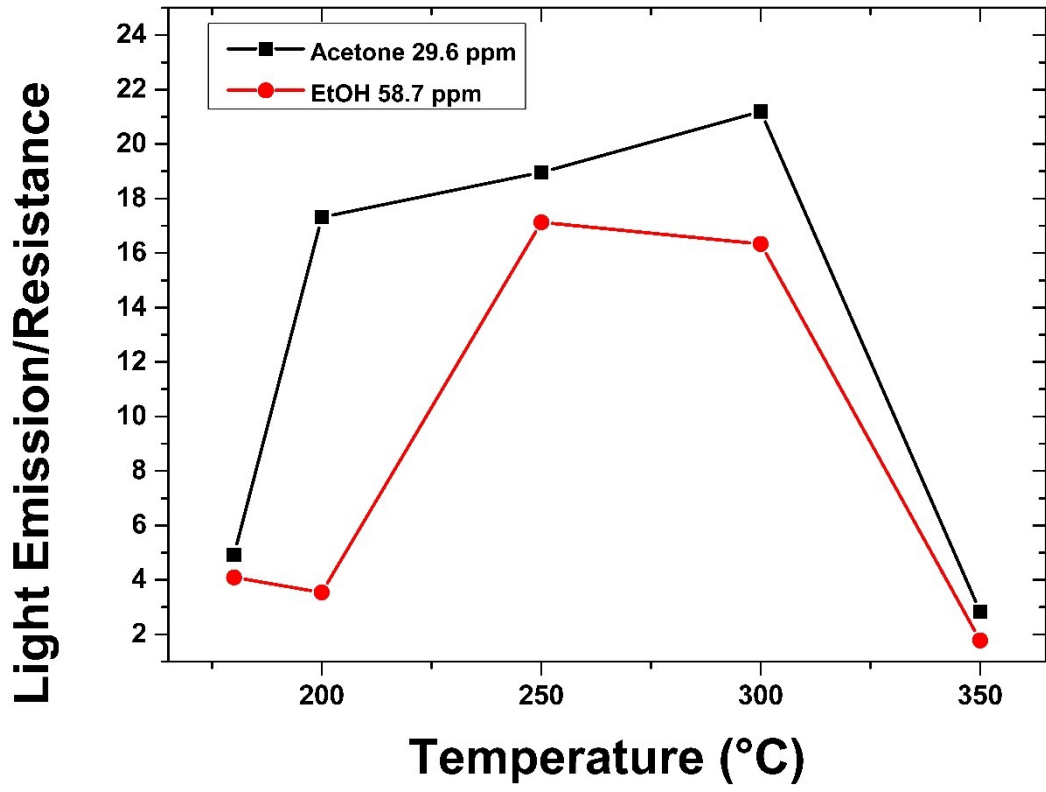
681



682

683 **Fig. 16**

684



685

686 **Fig. 17**

687

688

689

Supplementary Information

690

691 **Rare Earth Doped Metal Oxide Sensor for the Multimodal Detection of Volatile**

692 **Organic Compounds (VOCs)**

693

694 Matteo Fois, Timothy Cox¹, Norman Ratcliffe, Ben de Lacy Costello*

695 *Department of Applied Sciences, The University of the West of England, Bristol BS16*

696 *1QY, UK*

697 ¹*Institute of Biosensing Technology, The University of the West of England, Bristol*

698 *BS16 1QY, UK.*

699 **Corresponding author: Ben de Lacy Costello, Ben.DeLacyCostello@uwe.ac.uk*

700

701 **S1. Heater characteristics**

702 The basic dimensions of the heater side of the sensor are reported in Table S1.

703 Additionally, the heater resistance at room temperature is of 10 Ohms A scheme of the

704 heater is reported in Figure S1. The heater resistance at room temperature is of 10

705 Ohms.

706 *Table 1: Basic dimensions of the heater side of the sensor*

Sensor feature	Dimensions
Heater track width	180 μm
Gap between meanders	166 μm
Contact pad width	1175 μm
Contact pad length	500 μm

712

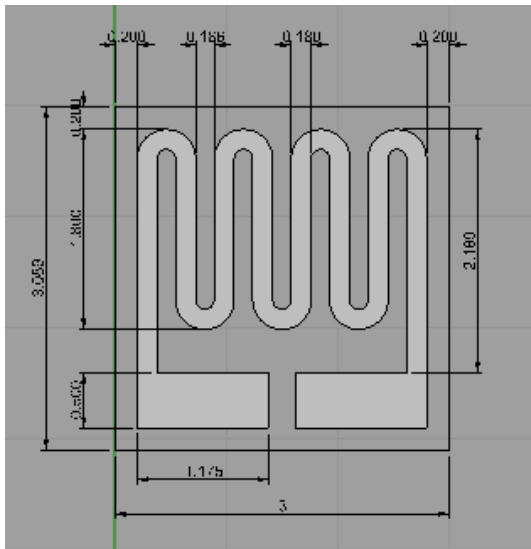


Figure 1 The heater employed during the eperiments

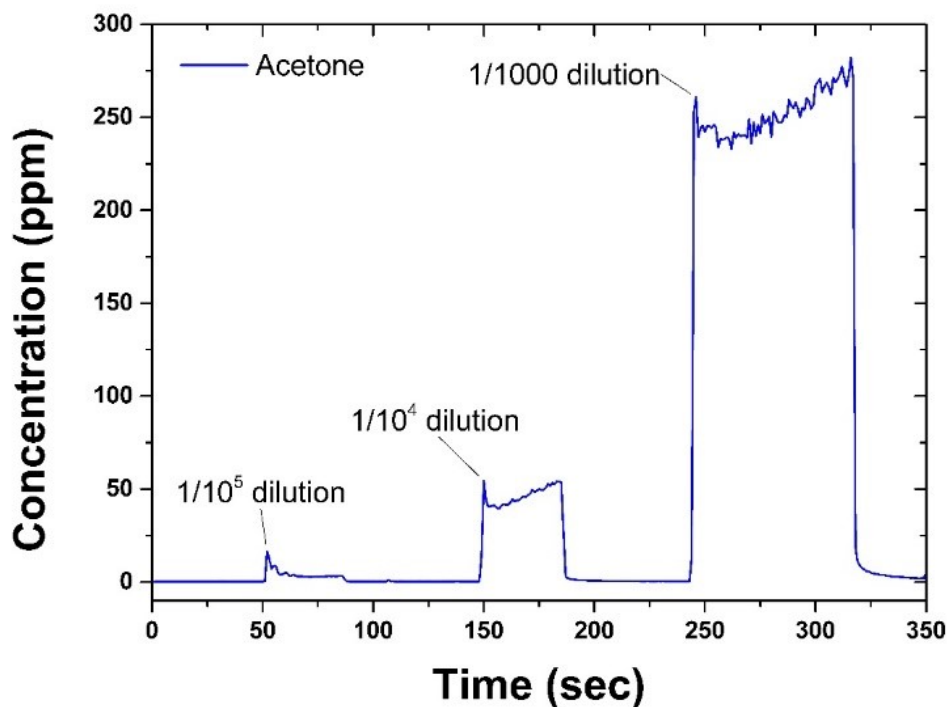
720

722 **S2. Dilution method validation: SIFT-MS**

723 In the sensing experiments, different volatile concentrations were obtained using a 10
724 mL gas-tight syringe. To check the efficiency of the method, the concentrations reported
725 in this paperwork were validated by selected ion flow tube (SIFT) mass spectrometry.

726 The SIFT-MS used for all the experiments is a Voice 200 (Syft technologies, New
727 Zealand). The sample inlet was set to the default flow rate of 30 mL/min, with the inlet
728 capillary and base both operating at 120°C. The dwell time for each mass was set to
729 1000ms or 100,000 counts depending on which was achieved first. Selected compounds
730 for this method was acetone.

731 Different increasing dilutions were carried out by a 10 mL gas-tight glass syringe and
732 injected into the machine. 1 mL of acetone headspace was taken from the vial. As a
733 matter of example, a dilution of 1/10 was obtained by taking this 1 mL to 10 mL by the
734 syringe and then coming back to 1 mL. Repeating the operation a second time allowed
735 getting a concentration of 1/100, repeating three times of 1/1000 and so on. The 1 mL of
736 the obtained concentration was then injected into the spectrometer. The results are
737 reported as raw data in Figure S2.

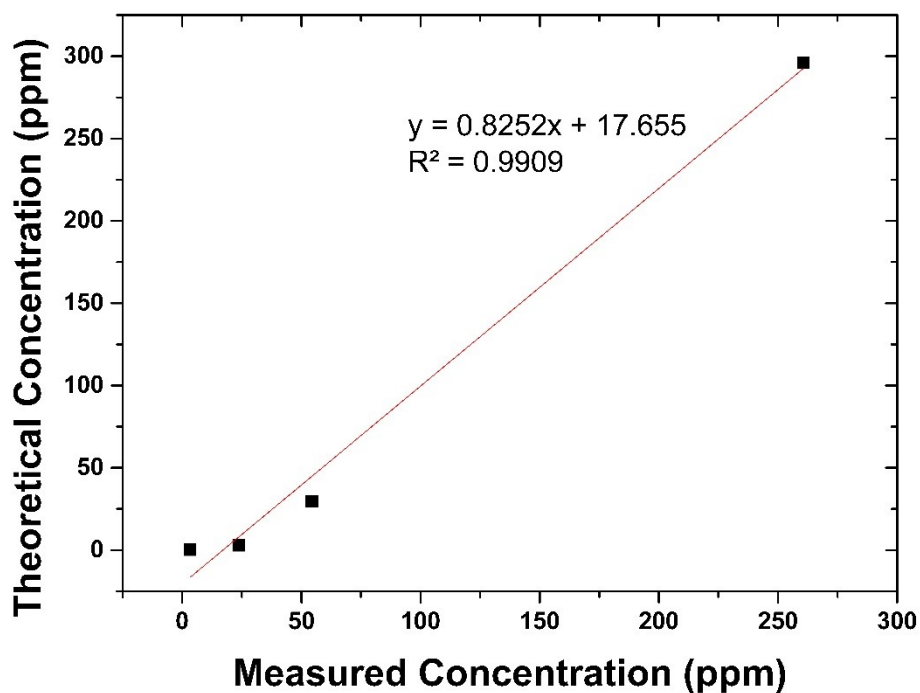


738

739 *Figure S2. Different levels of dilution, starting from the headspace concentration of acetone, registered*
 740 *by selected ion flow tube (SIFT) mass spectrometry.*

741

742 Also, it is possible to make a comparison between the expected values of acetone
 743 concentration expected by a given dilution, and the concentration effectively registered
 744 by the spectrometer. The slope obtained by linear regression of the SIFT-MS measured
 745 data vs the theoretical values of acetone concentration is reported in Figure S3. Four
 746 dilutions have been taken into account, and the data registered by the SIFT-MS
 747 spectrometry are in good correlation with the theoretical values calculated.



748

749

750 *Figure S3 Theoretical acetone concentration as a function of the concentration measured by SIFT-MS*
 751 *and carried out with the glass syringe-dilution method.*

752

753

754

755 **S3. The sensor**

756 The typical sensor utilized during the study is reported in Figure S3, where it is possible
 757 to observe the metal oxide nanopowder coating. In this case, a ZrO₂ nanopowder was
 758 used.



759

760 *Figure S5 Sensor substrate drop-coated with ZrO₂ nanopowder.*

761